The transition of dynamic rupture styles in elastic media under velocity-weakening friction

A.-A. Gabriel,[1] J.-P. Ampuero,[2] L. A. Dalguer,[1] and P. M. Mai[3]

[1]   Although kinematic earthquake source inversions show dominantly pulse-like subshear rupture behavior, seismological observations, laboratory experiments and theoretical models indicate that earthquakes can operate with different rupture styles: either as pulses or cracks, that propagate at subshear or supershear speeds. The determination of rupture style and speed has important implications for ground motions and may inform about the state of stress and strength of active fault zones. We conduct 2D in-plane dynamic rupture simulations with a spectral element method to investigate the diversity of rupture styles on faults governed by velocity-and-state-dependent friction with dramatic velocity-weakening at high slip rate. Our rupture models are governed by uniform initial stresses, and are artificially initiated. We identify the conditions that lead to different rupture styles by investigating the transitions between decaying, steady state and growing pulses, cracks, sub-shear and super-shear ruptures as a function of background stress, nucleation size and characteristic velocity at the onset of severe weakening. Our models show that small changes of background stress or nucleation size may lead to dramatic changes of rupture style. We characterize the asymptotic properties of steady state and self-similar pulses as a function of background stress. We show that an earthquake may not be restricted to a single rupture style, but that complex rupture patterns may emerge that consist of multiple rupture fronts, possibly involving different styles and back-propagating fronts. We also demonstrate the possibility of a super-shear transition for pulse-like ruptures. Finally, we draw connections between our findings and recent seismological observations.

1.   Introduction

[2]   Earthquake ruptures are thought to propagate in one of two basic styles, either as cracks or as pulses. During crack-like rupture the frictional strength of the fault suffers irreversible reduction, the fault slides simultaneously over the entire ruptured area and slip continues until arrest fronts arrive from the terminal edges of the rupture [*Kostrov*, 1964]. In this case, the local duration of slip, also known as risetime, scales with the shortest dimension of the final rupture area. In a pulse-like rupture, first postulated by *Brune* [1970], frictional strength weakens only transiently and the rupture front is closely followed by a healing front, which leads to short risetimes. Such short risetimes were first inferred from kinematic source inversions of natural earthquakes by *Heaton* [1990], and have been proposed to explain the complexity of seismicity patterns [*Cochard and Madariaga*, 1996] and the lack of heat flow anomaly on the San Andreas Fault [*Noda et al.*, 2009]. The estimation of risetime remains severely affected by the limited resolution and inherent non-uniqueness of kinematic source inversions [*Ide et al.*, 2005; *Page et al.*, 2011]. For instance, there are contrasting interpretations of rupture style from near-source ground motion recordings of the Mw 8.8 2010 Chile earthquake [*Madariaga et al.*, 2010; *Heaton et al.*, 2011]. Nonetheless, pulse-like rupture has been assumed or inferred in most source studies, with notable exceptions [*Yomogida*, 1988; *Campillo et al.*, 1989; *Peyrat et al.*, 2001; *Mavroeidis and Papageorgiou*, 2010; *Di Carli et al.*, 2010]. Despite the large body of theoretical, computational, experimental and seismological work on pulse-like rupture there are still outstanding questions, such as: What controls the speed of the healing front? How short are risetimes? What controls the selection between crack-like and pulse-like rupture at high background stress?

[3]   Several mechanisms for the generation of pulse-like rupture have been proposed: self-healing under velocity-dependent friction [*Heaton*, 1990], coupling between slip

[1]Swiss Seismological Service, Swiss Federal Institute of Technology Zurich, Zurich, Switzerland.
[2]Seismological Laboratory, California Institute of Technology, Pasadena, California, USA.
[3]King Abdullah University of Science and Technology, Thuwal, Saudi Arabia.

Corresponding author: A.-A. Gabriel, Swiss Seismological Service, Swiss Federal Institute of Technology Zurich, NO F69.3, Sonneggstr. 5, CH-8092 Zurich, Switzerland. (alice@sed.ethz.ch)

and dynamic normal stress changes in bimaterial faults [*Andrews and Ben-Zion*, 1997; *Ampuero and Ben-Zion*, 2008; *Dalguer and Day*, 2009], healing fronts induced by the spatial heterogeneity of fault strength and initial stress [*Beroza and Mikumo*, 1996; *Day et al.*, 1998; *Oglesby and Day*, 2002], by the finite thickness of the seismogenic zone [*Day*, 1982; *Johnson*, 1992] or by waves reflected inside a low-velocity fault zone [*Huang and Ampuero*, 2011]. The focus of our current work is on the first mechanism. Dramatic velocity-weakening at high slip rates is amply supported by laboratory experiments [e.g., *Tsutsumi and Shimamoto*, 1997; *Tullis and Goldsby*, 2003; *Di Toro et al.*, 2005; *Hirose and Shimamoto*, 2005] and by theoretical studies [*Rice*, 2006; *Beeler et al.*, 2008].

[4] That earthquakes can operate either as pulses or cracks, depending on the background fault stress, is likewise supported by laboratory experiments [e.g., *Xia et al.*, 2004; *Lykotrafitis et al.*, 2006; *Lu et al.*, 2007] and theory [e.g., *Cochard and Madariaga*, 1994; *Perrin et al.*, 1995; *Beeler and Tullis*, 1996; *Zheng and Rice*, 1998; *Nielsen and Carlson*, 2000; *Ampuero and Ben-Zion*, 2008; *Noda et al.*, 2009; *Dunham et al.*, 2011]. At low stress levels pulses are found to be the natural rupture style and crack-like propagation is impossible [*Zheng and Rice*, 1998; *Nielsen and Carlson*, 2000]. However, at intermediate stresses both styles are admissible and the selection depends, among several factors, on details of the chosen nucleation process, which is often artificially induced in experiments and simulations. Rupture patterns that depart from the basic crack and pulse dichotomy, for instance involving repeated slip episodes, have been observed in laboratory experiments [*Nielsen et al.*, 2010] and suggested from seismological observations [*Lee et al.*, 2011; *Yao et al.*, 2011]. One goal of the present work is to develop a comprehensive view of the role of nucleation, initial stress and velocity-weakening parameters on the selection of rupture style, including complex rupture patterns with multiple simultaneous rupture fronts and possible co-existence of pulses and cracks.

[5] Earthquake ruptures can propagate at sub-shear or at intersonic speeds [*Archuleta*, 1984; *Spudich and Cranswick*, 1984; *Dunham and Archuleta*, 2004; *Bouchon et al.*, 2010]. Theoretical and computational studies [*Andrews*, 1976; *Andrews*, 1985; *Dunham*, 2007] have quantified the conditions for supershear transition, including the role of initial fault stresses and friction law. However, these studies were essentially limited to cracks governed by slip-weakening friction. On the other hand, supershear pulse-like rupture has been observed in laboratory experiments [*Lu et al.*, 2007, 2009]. In the present work we explore the supershear transition for both cracks and pulses under velocity-weakening friction.

[6] Insights developed on the basis of idealized dynamic rupture models are fundamental to gain further understanding of earthquake mechanics, to ultimately enable realistic ground motion prediction for seismic hazard assessment, and to motivate further developments in observational seismology. The main goals of the present computational study are to identify the general rupture styles in which a fault can operate and to quantify the conditions for their occurrence. We aim at defining the dynamic rupture styles that are admissible under idealized conditions. We believe this fundamental study will provide building blocks of a framework

for the interpretation of more realistic rupture scenarios to be developed in ongoing and future studies.

[7] In section 2 we formulate an idealized model of rupture on a planar velocity-weakening fault with uniform initial stress and a smooth nucleation procedure. In section 3 we present the results of a broad parametric study of the effect of the initial shear stress, the nucleation size and the characteristic velocity for the onset of fast velocity-weakening. We present a diversity of dynamic rupture styles, which we classify as pulses or cracks, decaying or growing, sub-shear or super-shear, and single or multiple. We discuss their stability, macroscopic properties and conditions of existence. Relations to previous work and implications of our results are discussed in section 4.

2. Model Setup

2.1. Problem Formulation

[8] We model 2D in-plane spontaneous dynamic shear rupture in an isotropic linear elastic continuum with shear modulus μ, shear wave speed c_S, compressional wave speed c_P and Poisson's ratio ν. We represent the fault by a linear interface across which displacement discontinuity (slip) is allowed. Slip and stresses along the fault are related by a friction law. Frictional shear strength, τ_c, is proportional to the effective normal stress on the fault, σ (taken positive in compression): $\tau_c = \mu_f \sigma$, where μ_f is the friction coefficient. The absolute magnitude of shear traction on the fault, τ, is bounded by τ_c, $\tau \leq \tau_c$. If $\tau < \tau_c$ the fault remains locked. Sliding starts when the fault shear traction reaches the shear strength, $\tau = \tau_c$. During sliding the fault shear traction remains equal to the shear strength. The friction coefficient evolves as explained in the next section.

2.2. Friction Law

[9] Physical weakening processes due to thermal effects can operate on natural faults at slip velocities (V) typical of dynamic earthquake sliding [*Rice*, 2006]. In particular, flash heating can introduce severe velocity-weakening in the form of a $1/V$ behavior of frictional strength [*Rice*, 2006; *Beeler et al.*, 2008]. To represent such processes, we adopt a rate- and state-dependent friction law with fast velocity-weakening, as assumed by *Ampuero and Ben-Zion* [2008]. The friction coefficient is determined by the slip velocity and a state variable (Θ) as:

$$\mu_f = \mu_s + a\frac{V}{V + V_c} - b\frac{\Theta}{\Theta + D_c}, \qquad (1)$$

where μ_s is the static friction coefficient, V_c a characteristic velocity scale, D_c a characteristic slip scale and a and b are two positive coefficients that quantify a direct effect and an evolution effect, respectively. The state variable has units of slip and is governed by the following evolution equation:

$$\dot{\Theta} = V - \Theta\frac{V_c}{D_c}. \qquad (2)$$

The friction coefficient at steady state, i.e. when $\dot{\Theta} = 0$, is

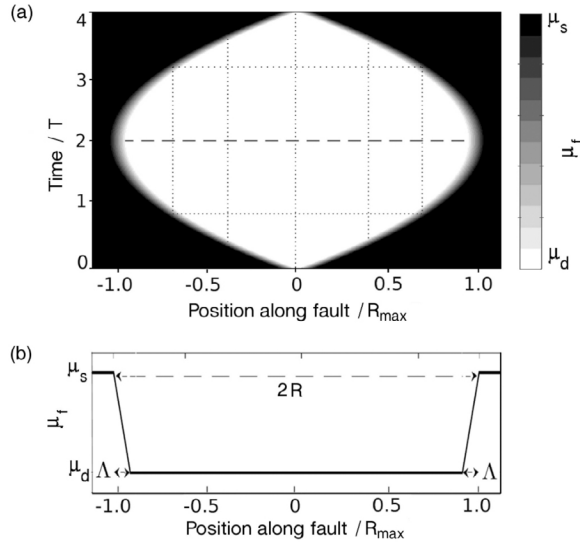$$\mu_f = \mu_s + (a - b)\frac{V}{V + V_c} \qquad (3)$$

Figure 1. Nucleation with healing. Prescribed time-weakening friction coefficient μ_f. (a) Spatiotemporal shape of nucleation area. Nucleation has duration $4T$ and propagates with decreasing speed from an initial value V_n. The nucleation zone reaches a maximum half-size $R_{\max} = V_n T$. (b) Prescribed spatial distribution of μ_f at $t = 2T$ during nucleation.

If $a < b$, the friction coefficient weakens asymptotically as $1/V$. In the limit of $V \gg V_c$, μ_f approaches the following dynamic friction coefficient

$$\mu_d = \mu_s + a - b \qquad (4)$$

over a relaxation timescale D_c/V_c. As described by *Ampuero and Ben-Zion* [2008], this relaxation time tunes the weakening mechanism between the two extreme behaviors, slip-weakening and velocity-weakening. The nominal strength drop $\sigma(\mu_s - \mu_d) = \sigma(b - a)$ is denoted τ_D.

2.3. Nucleation Procedure

[10] Observational constraints on earthquake initiation processes are elusive and earthquake simulations that incorporate spontaneous aseismic nucleation are computationally demanding. Hence, dynamic rupture simulations often adopt artificial nucleation procedures. Several studies have revealed that details of rupture initiation can significantly affect the subsequent rupture propagation [*Festa and Vilotte*, 2006; *Shi et al.*, 2008; *Lu et al.*, 2009; *Bizzarri*, 2010]. Here we assess the role of nucleation conditions in determining the rupture style by studying systematically the influence of the size of nucleation. We adopt a self-healing nucleation procedure introduced by *Andrews and Ben-Zion* [1997], which consists of a transient weakening process with subsequent healing. In Appendix A we consider a nucleation procedure without healing.

[11] We prescribe a nucleation region with time-dependent size, within which we force the friction coefficient to be smaller than a prescribed time-dependent value.

The nucleation region first expands and then contracts. Its half-size, R, is given by

$$R(t) = \begin{cases} V_n t \left(1 - \dfrac{t}{4T}\right) & \text{for } 0 \le t \le 4T \\ 0 & \text{for } t \ge 4T, \end{cases} \qquad (5)$$

where V_n is the initial rupture propagation speed and $4T$ the total duration of nucleation. The shape of the nucleation zone resulting from equation (5) is depicted in Figure 1a. Its maximum half-size is $R_{\max} = V_n T$. We found that simulations with same $R_{\max}$ but different V_n and T lead to similar rupture styles. In our simulations we evaluate the effect of nucleation by varying systematically the maximum nucleation half-size, $R_{\max}$. We prescribe the following spatial distribution of the friction coefficient as a function of position x along strike:

$$\mu_f = \begin{cases} \mu_s - \dfrac{(R - |x|)}{\Lambda}(\mu_s - \mu_d) & \text{for } R \ge |x| > (R - \Lambda) \\ \mu_d & \text{for } |x| < (R - \Lambda), \end{cases} \qquad (6)$$

where Λ is the along-strike length across which the friction coefficient drops from its static value μ_s to the dynamic one μ_d. The prescribed friction coefficient distribution is illustrated in Figure 1b.

[12] Within the nucleation region we keep updating the state variable Θ according to equation (2). We set the friction coefficient to the minimum between the prescribed time-dependent value (equation (6)) and the rate-and-state value (equation (1)). Spontaneous rupture propagation starts eventually once the frictional weakening becomes dominated by the rate-and-state evolution. Healing in the nucleation region is never faster than the prescribed time-weakening healing, but it may be slower when dominated by a slow evolution of Θ.

2.4. Initial Stresses

[13] The initial stresses on the fault are known to affect rupture style [*Zheng and Rice*, 1998] and rupture speed [*Andrews*, 1976]. However, their value in natural faults is uncertain. We consider here a broad range of initial stress values, assuming they are uniform along the fault. Due to the symmetries of the problem the normal stress remains constant. We quantify the initial shear stress by the dimensionless parameter S [*Das and Aki*, 1977a], the ratio of initial strength excess to (nominal) dynamic stress drop [see also *Andrews*, 1976]:

$$S = \frac{\tau_s - \tau_0}{\tau_0 - \tau_d} \qquad (7)$$

where $\tau_s = \sigma\mu_s$ and $\tau_d = \sigma\mu_d$ are the static and dynamic strengths, respectively, and τ_0 is the initial shear stress. The "relative strength" S (sometimes also referred to as "seismic ratio" [*Templeton and Rice*, 2008; *Kaneko and Lapusta*, 2010]) describes the strength of the material relative to the dynamic stress drop [*Das and Aki*, 1977b], and provides a measure of the closeness of the initial stress to the failure criterion.

[14] The value of the friction coefficient during sliding is μ_d under slip-weakening friction. However, it is generally higher than μ_d under velocity- and state-dependent friction

Table 1. Reference Simulation Parameters

Parameter	Description	Value
c_S	Shear wave speed	1
ν	Poisson's ratio	0.25
μ_s	Static friction coefficient.	0.6
μ_d	Dynamic friction coefficient.	0.1
a	Direct effect coefficient.	0.005
b	Evolution effect coefficient.	0.505
μ	Shear modulus	1
V_c	Characteristic frictional velocity scale	0.07
D_c	Characteristic frictional slip scale	1
σ	Background normal stress	2
τ_0	Background shear stress	0.4–1
Λ	Weakening length	1
V_n	Nucleation speed	0.5
X	Distance scaling factor	1
$\frac{x}{c_S}$	Time scaling factor	1
τ_D	Strength drop	1
h	Spectral element size	1
T	Nucleation duration	1–400
R_{max}	Nucleation half-size	0.5–200
S	Relative strength	0.25–4

and $\tau_0 - \tau_d$ is not an adequate estimate of the actual dynamic stress drop. Modified definitions of the relative strength parameter that account for this are presented in Appendix B.

2.5. Non-dimensional Units and Parameter Space

[15] Dimensional analysis shows that the problem formulated here depends on the following non-dimensional numbers: S, $R_{max}\tau_D/\mu D_c$, $\mu V_c/\tau_D c_S$, ν, a/b and V_n/c_S. This study is focused on the effect of the three first quantities. The remaining three are held fixed. Poisson's ratio ν is not expected to affect our results within the narrow range of its usual values. In fact, most of our conclusions, except the super-shear ruptures, hold also for anti-plane deformation (mode III), in which Poisson's ratio is irrelevant. We have verified that for a given maximum nucleation half-size, $R_{max} = V_nT$, the non-dimensional nucleation speed V_n/c_s is irrelevant as long as it is slow enough. The value of the non-dimensional parameter a/b is chosen small enough to have little impact on the rupture, but large enough to provide efficient regularization of the velocity-weakening friction, i.e. to yield a large enough critical wavelength [*Ampuero and Ben-Zion*, 2008] to be resolved numerically at an affordable computational cost.

[16] All parameters in this study are non-dimensional, making it possible to scale our results to a range of values of physical parameters such as D_c or initial stress, which in reality are poorly constrained. Stresses are scaled by the nominal strength drop, $\tau_D = \sigma(\mu_s - \mu_d)$, slip by the characteristic slip scale D_c, distances by $X = \mu D_c/\tau_D$, time by X/c_S and slip rates by $D_c c_S/X = \tau_D c_S/\mu$. A typical set of model parameter values, listed in Table 2 in real units, results in the following scaling factors: $\tau_D = 20$ MPa, $X = 10$ m, timescale 2.7 ms and slip rate scale 2 m/s.

[17] We conducted a large number of simulations which systematically explore the role of initial stress level (characterized by S) and nucleation size (R_{max}) in determining the rupture style. In Appendix A we additionally report on the effect of the type of nucleation procedure (with or without healing). Table 1 shows the explored range of S and R_{max}, and the fixed values of all the other model

parameters. The chosen range of S spans subshear and supershear rupture conditions in slip-weakening simulations [*Andrews*, 1976]. An upper bound for the static stress drop is $\tau_0 - \tau_d = \tau_D/(1 + S)$. The S values we explored (0.25 ~ 4) imply $\tau_0 - \tau_d = 4 ~ 16$ MPa, which is within the typical range of earthquake stress drops. We adaptively refined the values of the parameters S and R_{max} to capture the details of the transitions between rupture styles. The parameter space of this study is complementary to that of *Ampuero and Ben-Zion* [2008], who varied nucleation size and V_c while keeping initial stress constant ($S = 1.7$) in most of their work (except in their Appendix D).

[18] In most of our simulations we set the characteristic velocity of the friction law to $V_c = 0.07$ (non dimensional). This value leads to a variety of rupture styles in the study of *Ampuero and Ben-Zion* [2008]. Assuming the parameters of Table 2, this corresponds to $V_c = 0.14$ m/s. The value is higher if the assumed effective normal stress is larger. The slip velocity at the onset of severe thermal weakening induced by flash heating is of the order of 0.1 m/s for background temperatures at the middle depth of crustal seismogenic zones [*Rice*, 2006], and a plausible range is 0.05 to 2 m/s [*Beeler et al.*, 2008]. Significant weakening induced by thermal pressurization is possible at mid-seismogenic depth if slip rate exceeds $10/w$, where w is the thickness of the slip zone in microns, e.g. $V > 0.1$ m/s if $w = 100$ μm [*Wibberley and Shimamoto*, 2005]. *Nielsen et al.* [2008] observed weakening by frictional melt in laboratory experiments with a characteristic slip velocity in the range 0.04 to 0.14 m/s. Characteristic velocities in the range $V_c ~ 0.1$ m/s have been also inferred from seismological observations [*Nielsen and Olsen*, 2000]. In section 3.7 we explore the effect of V_c on rupture styles.

2.6. Numerical Method

[19] Our simulations employ a spectral element method for 2D wave propagation and source dynamics (SEM2D-PACK [*Ampuero*, 2008]), which solves for elasto-dynamic wave propagation coupled to frictional sliding along the fault. The spectral element method is a well established numerical method in seismic wave propagation [e.g., *Komatitsch and Vilotte*, 1998; *Komatitsch and Tromp*, 1999]. Its accuracy in solving rupture dynamics has been demonstrated in benchmark problems [*Kaneko et al.*, 2008; *Harris et al.*, 2004; *Huang and Ampuero*, 2011]. The equations of motion are solved by an explicit time stepping algorithm. The fault boundary conditions are handled as in the "tractions at split nodes" method [*Andrews*, 1999; *Kaneko et al.*, 2008]. The fault discontinuity is surrounded by a thin layer of Kelvin-Voigt material to damp spurious high-frequency oscillations [*Day and Ely*, 2002; *Dalguer and Day*, 2007].

Table 2. Example Parameters

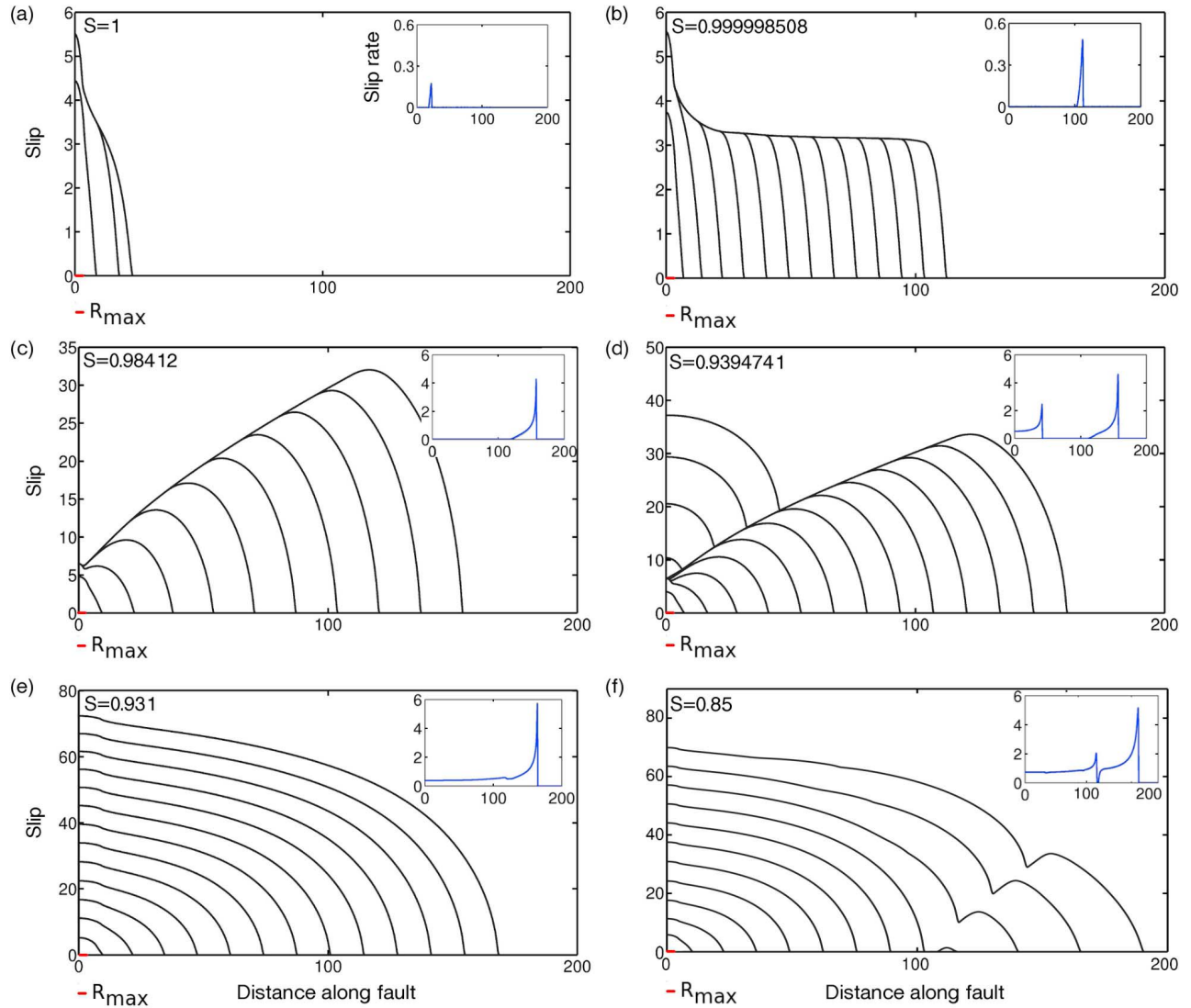| Parameter	Description	Value
c_S	Shear wave speed	3700 m/s
μ	Shear modulus	37 GPa
D_c	Characteristic slip scale	5.4 mm
σ	Background effective normal stress	40 MPa
τ_0	Background shear stress	8–20 MPa

Figure 2. Typical rupture styles. Spatial distribution of slip at regular times and a snapshot of slip rate as inset for (a) a decaying pulse, (b) a steady state pulse, (c) a growing pulse, (d) a superposition of a pulse and a crack, (e) a subshear crack, and (f) a superposition of a subshear crack and a supershear crack. Figures 2b, 2d, and 2f are transitional rupture styles separating rupture styles in Figures 2a, 2c, and 2e, respectively. The maximum nucleation half-size $R_{\max} = 4.4925$ is indicated by a red line in the bottom left of each plot.

[20] To avoid the effect of spurious wave reflections from the imperfect absorbing boundaries we set the domain size to conservatively large values. For a total simulation time t, the conservative domain size in the fault-normal direction is $w_{cons} = c_P t/2$, where c_P is the P wave velocity. In the along-strike direction it is $l_{cons} = (c_P + c_R)t$ for subshear ruptures and $l_{cons} = 2c_P t$ for supershear ruptures, where c_R is the Rayleigh wave speed.

[21] We set the spectral element size to $h = 1$ and the polynomial order to $p = 5$, i.e. 6×6 Gauss-Lobatto-Legendre (GLL) nodes per element and $\Delta x = 0.2$ average spacing between GLL nodes. We verified that these settings allow the cohesive zone to be resolved by at least 5 GLL nodes in all our simulations. During this study we performed several thousands of simulations to finely resolve the parameter space. Non-dimensional durations and domain

sizes ranged from 200 to 1000 and 550 to 2650, respectively. The largest simulations required 18 hours of single core CPU time and produced 100 GB of data per run.

3. Results

[22] Our simulations span a variety of rupture styles that we classify as decaying or sustained, pulses or cracks, subshear or super-shear, single or multiple ruptures. The first aim of our study is to determine the range of initial conditions (relative strength S and maximum nucleation half-size $R_{\max}$) that lead to each of these rupture styles. The effect of V_c is addressed only in section 3.7. Our second aim is to characterize, as a function of background shear stress, the rupture properties that do not depend on the details of nucleation.
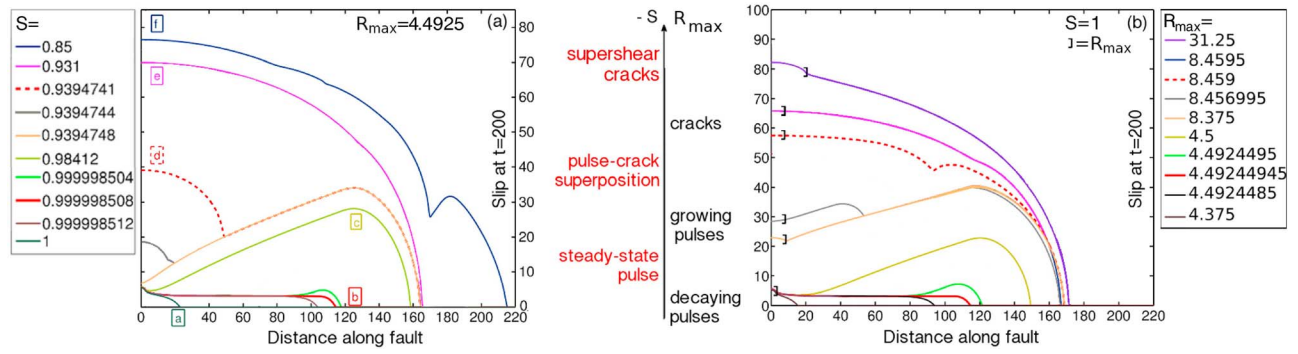
Figure 3. Rupture styles and their transitions as a function of S (Figure 3a) or R_{max} (Figure 3b). (a) Slip profiles at $t = 200$ for simulations with fixed $R_{max} = 4.4925$ and varying relative strength S. Each curve corresponds to a different value of S indicated in the legend. Transitional styles are highlighted and are also summarized on the central S scale. The steady state pulse (solid line) separates decaying and growing pulses. Superpositions of a primary pulse and a secondary crack nucleated at the hypocenter appear in an intermediate regime between pure pulses and pure cracks. The labels a–f correspond to the examples shown in Figure 2. (b) Same plot for simulations with fixed $S = 1$ and varying R_{max} (see the legend). Note the appearance of a secondary steady state pulse at $R_{max} = 8.456995$. The maximum half-size of the nucleation zone, R_{max}, is indicated by squared brackets for each simulation.

3.1. Overview of Effects of Initial Stress and Nucleation Conditions on Dynamic Rupture Styles

[23] We fixed R_{max} to the minimal value that allows self-sustained rupture with $S = 1$, and then ran a series of simulations with varying values of S. We observe three main rupture styles: decaying pulses at high S, growing pulses at lower S, and cracks at even lower S. Figures 2a, 2c, and 2e show the spatial distribution of slip at regular times typical of these three rupture styles. The insets show a typical snapshot (spatial distribution at a selected time) of slip rate for each simulation. Pulses are distinguished from cracks by the vanishing slip rate in the hypocentral region, induced by healing after the passage of the rupture front. Growing pulses generate triangular slip profiles with an elliptical cap at the leading front and cracks generate elliptical slip profiles. "Transitional" styles are also shown in Figure 2. Steady state pulses, characterized by flat slip profiles (Figure 2b), are the natural transition between decaying and growing pulses. In a narrow range of S, between growing pulses and cracks, ruptures involve the superposition of a primary pulse and a secondary crack nucleated at the hypocenter (Figure 2d). Ruptures that do not involve such feature will be called "pure pulses" or "pure cracks." At low S, cracks trigger, near their rupture front, a secondary pulse that travels at supershear speed (Figure 2f).

[24] Figure 3 summarizes all rupture styles found in this set of simulations by showing slip at the (arbitrary) simulation time $t = 200$ (each curve corresponds to a different simulation with a different value of S). The transitions between decaying and growing pulses, between pulse-crack superposition and pure cracks and between sub- and supershear ruptures occur at very specific values of S and are highlighted in Figure 3a. We finely tuned the value of S to find these transitional ruptures, following ad hoc procedures described later. The precision of S reported in Figure 3 reflects the extreme sensitivity of transitional styles to changes in initial conditions.

[25] In a second group of simulations we set $S = 1$ and varied the maximum nucleation half-size R_{max}. Slip at time $t = 200$ is shown in Figure 3b for all these simulations. The same sequence of rupture styles can be identified, driven now by increasing values of R_{max}, from decaying pulses to growing pulses to cracks. We tuned R_{max} to capture the transitional rupture styles. The evolution of rupture speed for a range of examples of different rupture styles (Figure 4) clearly shows the transitions from decaying to growing pulses and from subshear to supershear rupture.

[26] We ran a large set of simulations spanning the parameter ranges $0.25 \leq S \leq 4$ and $0.5 \leq R_{max} \leq 200$. At high values of S and R_{max}, we increased the simulation time and computational domain to fully capture the rupture style transitions. The conditions leading to each of the rupture styles found in our simulations are summarized in Figure 5. This "phase diagram" shows the locus in parameter space
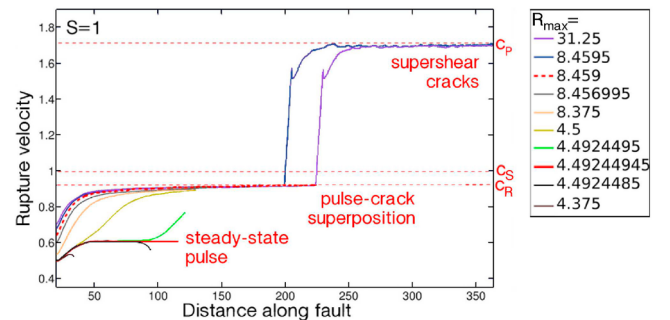

Figure 4. Evolution of rupture velocity v_r as a function of rupture propagation distance for different rupture styles with self-healing nucleation of varying maximum half-size R_{max} and $S = 1$. Transitional styles are highlighted. Steady state pulses propagate with $v_r \approx 0.6c_S$, growing pulses and cracks with $v_r \approx c_R$ (Rayleigh speed) and supershear ruptures with $v_r \approx c_P$.
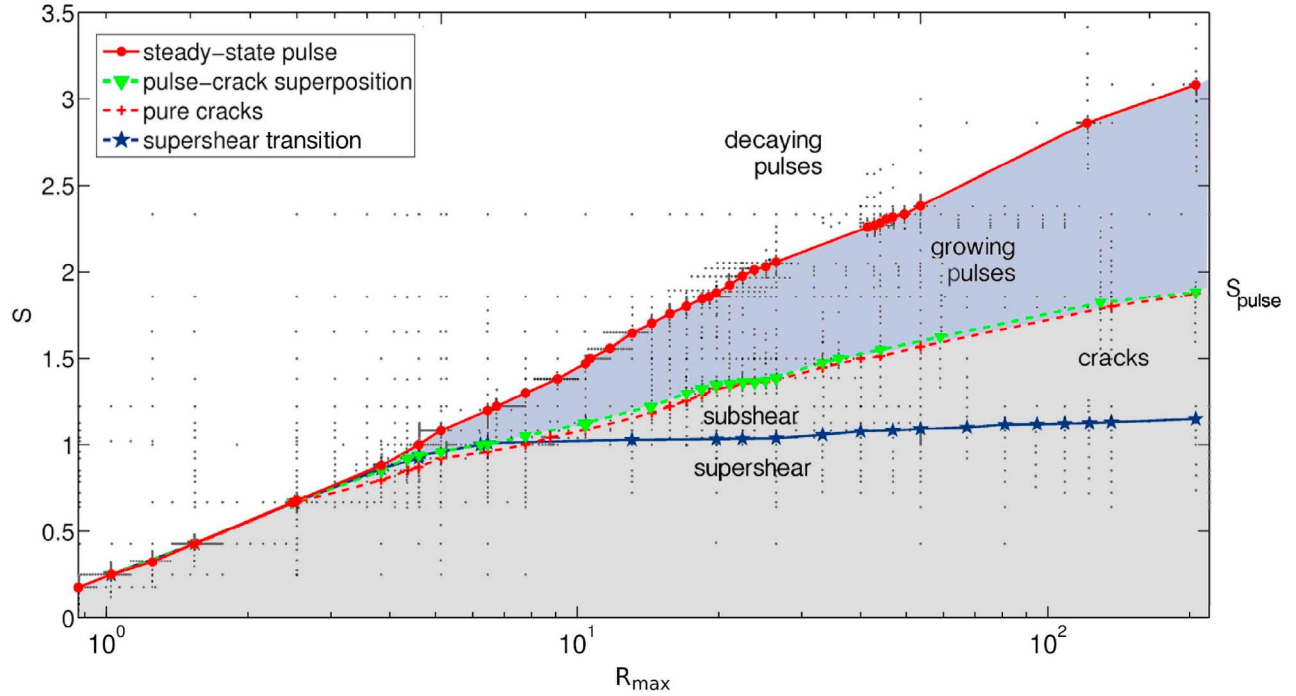
Figure 5. Summary of rupture styles as a function of S and R_{max} after nucleation with prescribed healing. Each small dot indicates one simulation out of a total of about 450 simulations carried out to compose this diagram. The curves indicate the S, R_{max} conditions at the transitions between rupture styles in order of appearance in the legend: transition between decaying and growing pulses (steady state pulse), transition between pure pulses and mixed pulse-crack ruptures, transition between pulse-crack superpositions and pure cracks, transition between subshear and supershear ruptures (when supershear happens at $t < 1000$). Along most transition boundaries R_{max} depends roughly exponentially on S. The theoretical maximum S that allows cracks [*Zheng and Rice*, 1998] is indicated as S_{pulse}. The maximum S that allows supershear ruptures is close to 1 and depends weakly on R_{max}.

(R_{max} and S) of the transitional rupture styles that separate decaying pulses, growing pulses, pulse-crack superimposed ruptures and pure cracks, as well as sub- and supershear ruptures. The diagram focuses only on the rupture style transitions of the primary front. These boundaries are sharp: a slight change of R_{max} or S can dramatically transform a rupture style. Along the transition boundaries R_{max} depends roughly exponentially on S. If S is increased less potential energy is available and all rupture style transitions require higher nucleation energies, which is provided by larger R_{max}. The transition boundaries approach each other at decreasing S, which necessitates even finer tuning. Figure 5 indicates a "supershear transition" for the largest value of S at a given R_{max} that enables supershear ruptures in long simulations of duration $t = 1000$. This critical S for supershear transition depends on R_{max} and, for large enough R_{max}, it is close to 1.2.

[27] In Appendix A we ran the same set of simulations applying a non-healing nucleation procedure. We found that the nucleation type does not affect significantly the rupture transition processes.

[28] In the following, all transitional and stable rupture regimes are characterized in more detail.

3.2. Transition Between Decaying and Growing Pulses: Steady State Pulses

[29] The steady state pulses in this study are defined, far from the nucleation region, by spatially uniform rupture
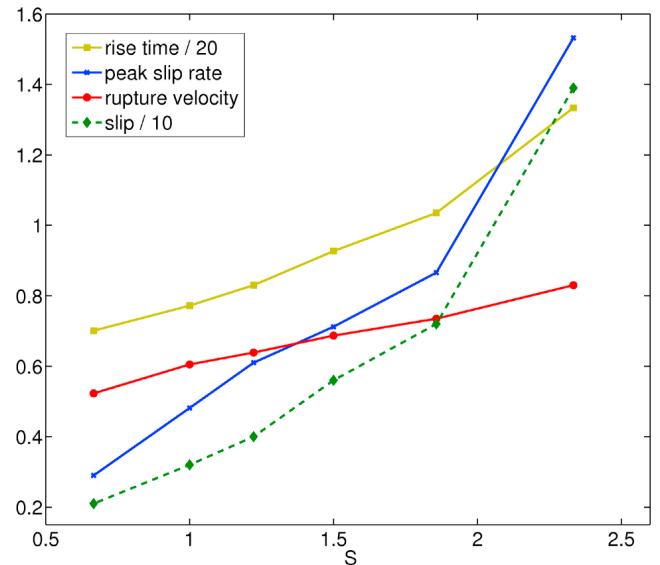

Figure 6. Properties of steady state pulse-like ruptures. Slip, peak slip rate, risetime and rupture velocity during steady state pulse propagation as a function of relative strength S.
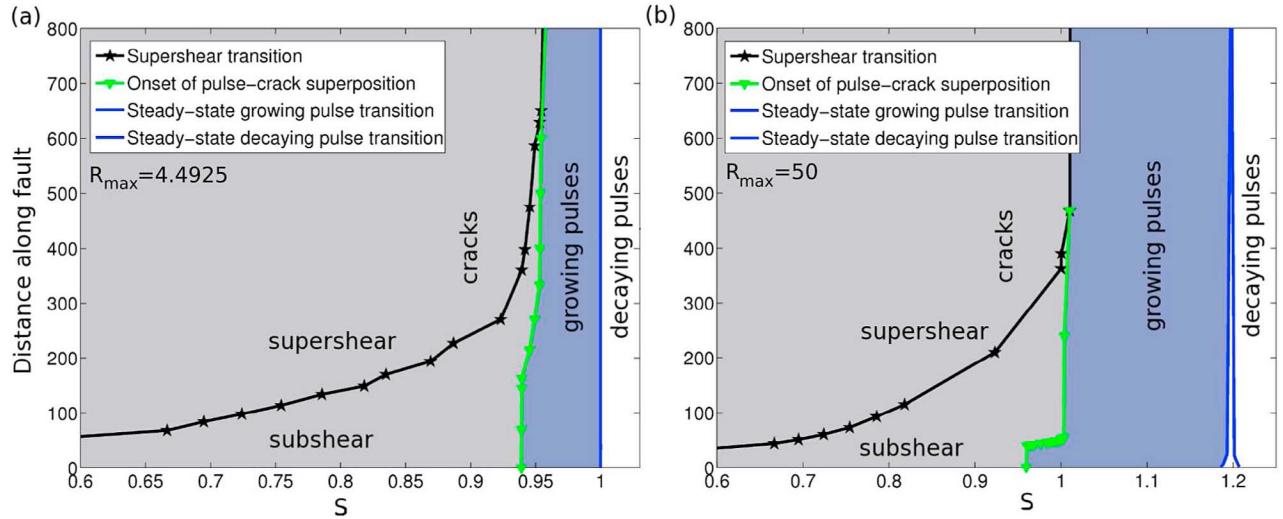
Figure 7. Transition distances for supershear transition, the onset of pulse-crack superposition and steady state transition, as a function of S for (a) R_{max} = 4.4925 and (b) R_{max} = 50.

speed (Figure 4), peak slip rate, and risetime. Their passage leaves a spatially uniform slip (Figure 2b). Their rupture speed, peak slip rate, risetime and cumulated slip increase as a function of S (Figure 6). Steady state pulses may propagate at low speeds, e.g. $v_r \approx 0.6c_S$ if $S = 1$ (Figures 4 and 6). These steady state pulses exist only for specific combinations of S and R_{max} values. For slightly different values, pulses initially run in steady state but then transform into dying or growing pulses. The departure from steady state happens sharply at a "transition distance" that depends strongly on the initial conditions. The transition distance diverges as the conditions for steady state rupture are approached (see the blue solid lines in Figure 7 [*Ampuero and Ben-Zion*, 2008, Figure 7]). The transitional S and R_{max} values in Figures 3a and 3b, respectively, lead to steady state propagation at least up to $t = 200$. Finer tuning is necessary to propagate a steady state pulse over longer times (as in Figure 5).

[30] The properties of steady state ruptures do not depend on the nucleation procedure nor on the ultimate fate of the

pulse (decay or growth) as long as they are measured during a sufficiently stable steady state portion of the rupture.

3.3. Growing Pulses

[31] Growing pulses occur in a range of parameter space (R_{max} and S) bounded at small R_{max} by steady state pulses and at large R_{max} by the onset of pure cracks if S is lower than a certain value $S_{pulse} \approx 1.95$ (Figure 5). Although the growing pulse regime is the dynamically stable rupture style requiring the shortest nucleation size, the condition for its existence is extremely narrow when $S < S_{pulse}$. High initial stress thus favors crack-like rupture.

[32] All growing pulses approach an almost self-similar asymptotic behavior [*Nielsen and Carlson*, 2000] with properties that depend on S but not on R_{max}. The asymptotic growing pulses have the following characteristics: constant slip gradient (Figures 3), constant rupture speed (Figure 4), constant healing front speed, and risetime proportional to rupture propagation distance. Figures 8a and 8b summarize
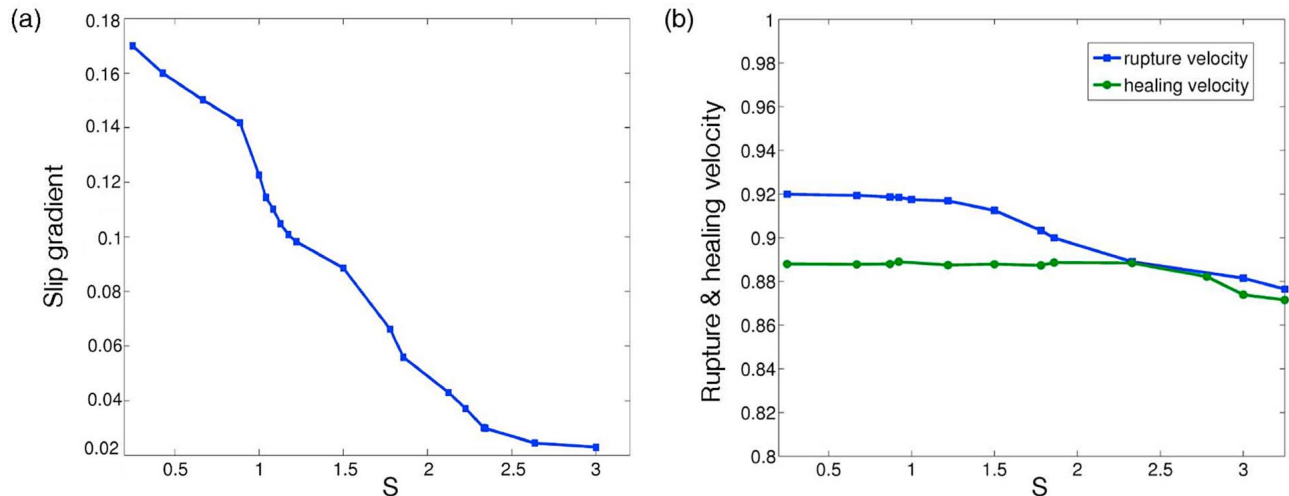

Figure 8. Asymptotic properties of growing pulses as a function of S: (a) gradient of slip and (b) rupture and healing front velocities.
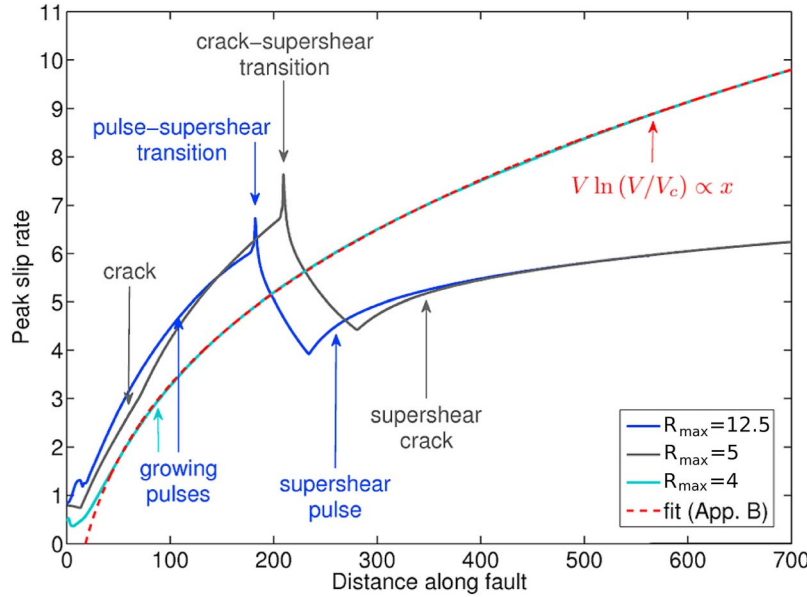
Figure 9. Peak slip rate evolution for a growing pulse, a crack, a supershear secondary crack and a supershear secondary pulse. Examples for $S = 0.923$ and R_{max} given in the legend. The growth of peak slip rate V as a function of rupture propagation distance x is consistent with a prediction based on fracture mechanics arguments (fit shown for the growing pulse example), see Appendix C.

the slip gradient, rupture speed and healing front speed as a function of S. Slip is accumulated faster at lower S. Growing pulses progressively accelerate toward the Rayleigh speed. This acceleration is slower at higher S, yielding lower rupture speeds at higher S for a given simulation time. The speed of the healing front is lower than the Rayleigh speed (Figure 8b) and depends little on S. What controls the speed of the healing front is one of the aspects of the dynamics of rupture pulses that remains poorly understood. Nevertheless, peak slip rates (V) do not approach a constant limit, as perfect self-similarity would require [*Nielsen and Madariaga*, 2003], but grow as a function of hypocentral distance x (Figure 9). As expected from fracture mechanics considerations (Appendix C), this growth is consistent with a relation of the form $V ln(V/V_c) \propto x$. This is illustrated in Figure 9 for $S = 0.923$ and $R_{max} = 4$. During supershear and crack-like ruptures the peak slip rate growth has a similar shape but is slower (Figure 9).

3.4. Transition From Pure Pulse to Pulse-Crack Superposition

[33] Growing pulses gradually concentrate stress in their hypocentral region. After a certain propagation distance, this stress concentration overcomes the fault strength and reactivates slip at the hypocenter, resulting in nucleation of a secondary rupture front. Figure 10 shows the evolution of slip rate and incremental shear stress along the fault for a growing pulse that triggers a secondary crack. Figure 11a shows another example.

[34] The rupture style of the secondary front is controlled by the overall amplitude of the "primary residual stress," i.e. the stress left behind by the primary pulse. Secondary ruptures are cracks in most of our simulations because the primary residual stress is often large over a broad area near the hypocenter. Secondary cracks typically run at near-Rayleigh
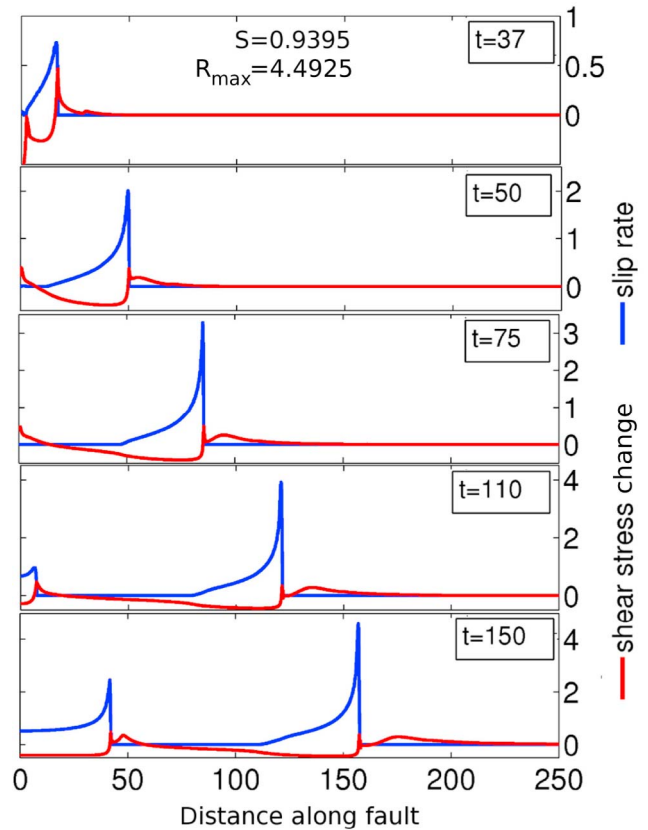

Figure 10. Pulse-crack transition. Spatial distribution of slip rate (blue) and shear-stress (red) at different times (indicated on the right of each plot) for an example of a growing pulse that triggers a crack at the hypocenter (case $S = 0.9395$ and $R_{max} = 4.4925$).
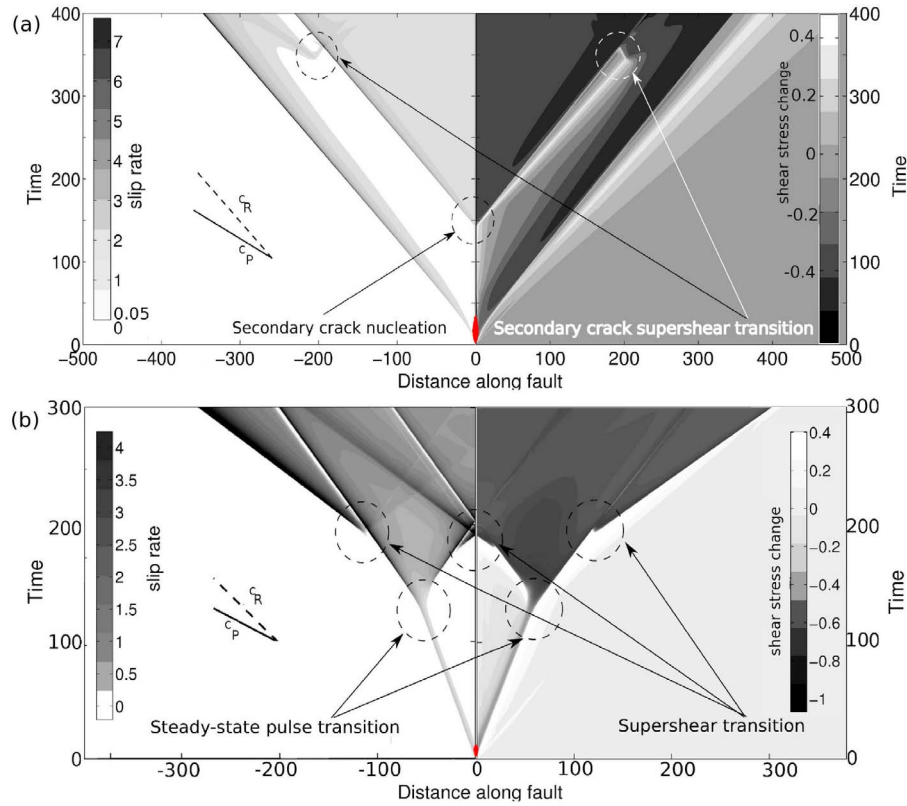
Figure 11. Nucleation of multiple sub- and supershear fronts. Spatiotemporal evolution of slip rate (left) and shear stress change (right). Nucleation areas are marked in red. (a) A growing pulse triggers a subshear crack at $t \approx 150$, which in turn nucleates a supershear crack at $t \approx 350$ (case $S = 0.9394$ and $R_{max} = 4.4925$). (b) A steady pulse transitions into an asymmetric bilateral crack at $t \approx 135$, which in turn nucleates super-shear cracks at its forward- and back-propagating fronts (case $S = 0.67$ and $R_{max} = 2.38$).

rupture speed (Figure 11a at $t < 350$), but if the primary residual stress is high enough they turn supershear (see section 3.6) and eventually coalesce with the primary front (Figure 11a at $t \approx 400$). In contrast, if the primary residual stress is low then the secondary rupture is a pulse. Secondary pulses have a steady state transition similar to that of primary pulses. One example of a growing pulse followed by a secondary steady state pulse is the case $S = 1$ and $R_{max} = 8.456995$ in Figure 3b. At higher S or longer R_{max} the secondary pulse is a growing one. A secondary growing pulse may, through the same residual stress concentration mechanism, trigger a third rupture front. Conceivably, the process can repeat, leading to a sequence of multiple pulses.

[35] The triggering mechanism is largely independent of R_{max} but depends on S. It operates over a narrow range of S and is impeded by other transition processes. The efficiency of the secondary triggering process depends on the spatial distribution of the primary residual stresses, hence on the smoothness of the slip left behind by the primary pulse. In particular, the rate of build up of the primary residual stress concentration correlates with the gradient of slip left by the primary pulse, which is lower at lower stress drop/higher S (Figure 8a). Hence the "transition distance" that a pulse needs to propagate to trigger a secondary rupture at the hypocenter increases as a function of S (green solid lines in Figure 7). The S-dependence of the transition distance is

steeper at low and high S. At low S, the efficient stress transfer to the hypocenter prevents healing and promotes the transition to crack-like behavior of the primary front. Primary cracks do not concentrate stress at the hypocenter. At high S, the nucleation size R_{max} required for growing pulses is long and might interfere with the stress build up. More significantly, primary pulses are preceded by a transient phase of steady pulse propagation. Their primary residual stress concentrates near the location of the transition to pulse growth, which can be offset at considerable distance from the hypocenter.

[36] While delayed pulse growth prevents nucleation at the hypocenter, secondary triggering can still happen away from the hypocenter and lead to complex rupture patterns. Figure 11b shows an initial steady pulse that starts to grow at $t \approx 130$. The emerging growing pulse rapidly concentrates stresses near its origin, at $x = 50$, and eventually triggers a back-propagating front. In this particular example, triggering happens before the passage of the healing front of the primary pulse, and the growing pulse rupture transforms into a bilateral crack.

3.5. Transition to Pure Cracks

[37] Cracks do not exist if S is larger than a certain critical value $S_{pulse} = 1.95$ (Figure 5). This is well explained by the "understressing theory" [*Perrin et al.*, 1995; *Zheng and Rice*, 1998], which for the friction law and friction parameters
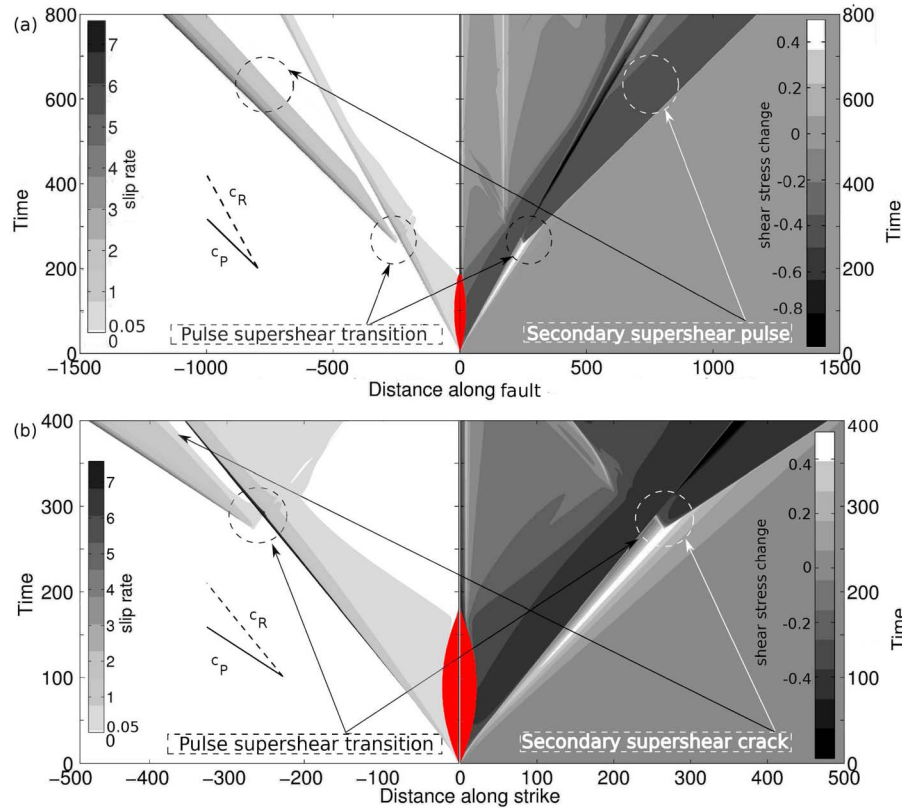
Figure 12. Supershear ruptures triggered by a primary pulse. Spatiotemporal evolution of slip rate (left) and shear stress change (right). Nucleation areas are marked in red. The resulting supershear rupture can be (a) a pulse, as shown for the case $S = 1$ and $R_{max} = 25$, or (b) a crack as shown for the case $S = 1$ and $R_{max} = 10.63$.

adopted here predicts that a minimum stress $\tau_{pulse} = 0.54$ is necessary for crack-like rupture. Below S_{pulse}, our simulations illustrate that the selection between cracks and pulses, and their coexistence, has a non trivial dependence on initial conditions.

[38] The transition between pulses and cracks involves complex rupture patterns with multiple fronts. With decreasing S and increasing R_{max}, the separation between the healing front of the primary pulse and the rupture front of the secondary rupture shortens and eventually disappears. This defines the transition to pure cracks. The coexistence of cracks and pulses, combined with nucleation effects complicate the definition of this transition. At high stresses ($S \ll 1$), the distance required to trigger a secondary rupture is small and all ruptures, apart from decaying and steady state pulses, can be essentially classified as cracks.

3.6. Supershear Rupture Transition

[39] Figure 4 shows examples of cracks whose rupture speed approaches the Rayleigh speed and eventually jumps to values faster than the S wave speed. This supershear transition is due to the "daughter crack" mechanism described by *Andrews* [1976] for cracks governed by slip-weakening friction: supershear fronts are triggered by the gradual build-up of a dynamic stress peak traveling at the S wave speed, ahead of the primary rupture front.

[40] Although in most of our simulations supershear ruptures are triggered by cracks, we found that pulses can also nucleate supershear fronts. Two examples are shown in Figures 12a and 12b. The supershear transition of pulses happens under a narrow range of conditions, as indicated by the small overlap between the S, R_{max} conditions for pulses and supershear ruptures in the phase diagram of Figure 5.

[41] The supershear transition is enabled and enhanced by high background stresses [*Andrews*, 1976]. The rupture propagation distance at which it occurs increases as a function of S and diverges around a critical value S_{ss} (see the black curves with stars in Figure 7).

[42] We found that $S_{ss} \approx 1$ for cracks and pulses, with a mild dependence on R_{max} (dashed curves with stars in Figure 5).

[43] Figure 13 shows the evolution of rupture speed of typical supershear ruptures with S and R_{max} close to the supershear transition boundary of Figure 5. Their rupture speed is close to c_P and decreases only slightly as a function of S, by less than 2%. This holds also when S and R_{max} are further away from the supershear transition. Moreover, the rupture speed of supershear fronts is independent of the rupture style of the primary (subshear) and secondary (supershear) fronts. For instance, in Figure 13 the final rupture speed of the three examples with $S = 1$ is very similar despite their different rupture styles.

[44] The supershear daughter ruptures triggered by pulses may propagate either as pulses or as cracks, as shown in Figures 12a and 12b, respectively. When the daughter rupture is crack-like, its back-propagating front may be sub-
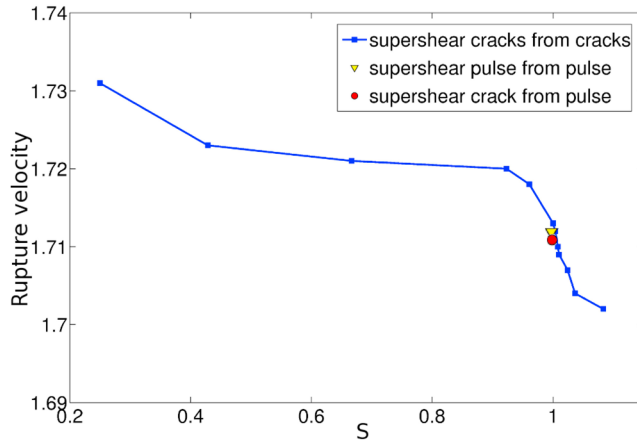
Figure 13. Rupture velocity of supershear fronts. Final rupture speed as a function of S in supershear ruptures with S and R_{max} close to the supershear transition boundary of Figure 5. Also shown are a supershear pulse and a supershear crack from a primary pulse at $S = 1$. The final rupture speed is close to the P wave speed and decreases slightly with increasing S. The styles of the primary and supershear ruptures do not affect rupture speed.

shear or super-shear, depending on the stress level left behind by the primary pulse (low or high, respectively). Figure 11b shows a steady state pulse that eventually transforms into a bilateral crack and then triggers a supershear daughter crack at its front. The back-propagating front of the daughter crack becomes supershear when it enters the higher stress regions left by the steady state pulse.

[45] Peak slip rate increases sharply at the onset of the supershear transition (Figure 9). This is due to the coalescence of the main rupture front and the back-propagating front of the daughter crack. Peak slip rate then decays to values lower than during the initial subshear propagation: the strength drop in the subshear front vanishes as most of the frictional weakening occurs in the supershear front.

Subsequently the peak slip rate at the supershear front increases. The asymptotic properties of supershear ruptures, such as peak slip rate and rupture velocity, do not depend on nucleation size (see the varying R_{max} in Figures 4 and 6) and are similar for supershear ruptures nucleated by primary and secondary ruptures.

[46] Secondary ruptures may also nucleate supershear fronts. Figure 11a shows a secondary crack, nucleated at the hypocenter, that eventually turns supershear. This rupture behavior is an additional feature to the supershear transition of the primary rupture front (Figure 7).

[47] The supershear transition of a pulse and the reactivation of slip at the hypocenter can interfere. At high R_{max} and low S the back-propagating front of a supershear crack removes the stress concentration at the hypocenter and hence prevents slip reactivation. Conversely, a secondary crack nucleated at the hypocenter may turn supershear and eventually overtake the primary pulse front impeding its supershear transition (Figure 11a).

3.7. Influence of Characteristic Weakening Velocity on Rupture Styles

[48] In the simulations we have presented so far we assumed that the characteristic velocity of the friction law (equation (1)) is $V_c = 0.07$ (normalized by $\tau_D c_S/\mu$). As discussed in section 2.5, this parameter may span a broad range of values in natural faults. We hence performed a set of simulations with different V_c values.

[49] At given S and R_{max}, changing V_c produces the same rupture style transitions as in our previous simulations. Figure 14a shows transitions driven by a decrease of V_c from decaying to growing pulse (through steady state) and finally to crack. This behavior is in general agreement with the results in *Ampuero and Ben-Zion* [2008, section 3.1]. Decreasing V_c increases the velocity-weakening rate, and hence reduces the effective nucleation size which in turn induces the transition to growing pulses. It also increases S_{pulse} [*Nielsen and Carlson*, 2000; *Ampuero and Ben-Zion*, 2008], which promotes the transition from pulses to cracks. Figure 14b summarizes the conditions of occurrence of each
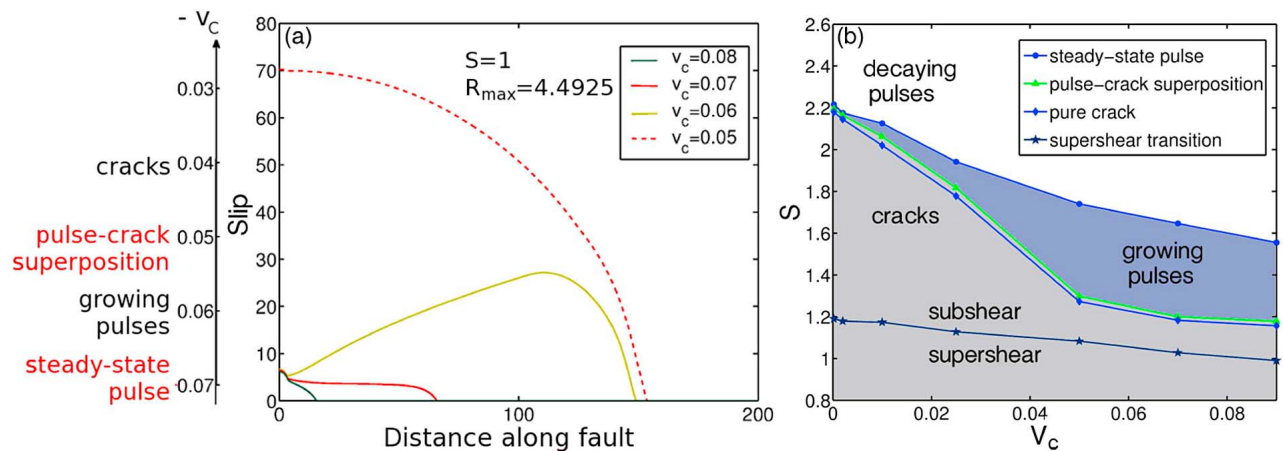

Figure 14. Rupture styles as a function of the characteristic slip velocity V_c of the velocity-weakening friction law. (a) Slip at time $t = 200$ for ruptures with $S = 1$, $R_{max} = 4.4925$ and different values of V_c indicated in the legend. The rupture style transitions are summarized along the V_c scale on the left. (b) Conditions for rupture style transitions as a function of S and V_c for $R_{max} = 4.4925$.

rupture style transition in terms of S and V_c, at fixed $R_{max} = 4.4925$. A reduction of V_c affects the phase space of rupture style transitions in a predictable way: decreasing V_c increases all transitional values of S. The critical S for supershear rupture is only weakly affected by V_c and remains well below the critical value $S = 1.77$ of linear slip-weakening friction. S_{pulse} increases with decreasing V_c as expected from the analysis of [*Zheng and Rice*, 1998]. At very low V_c the S-range of existence of pulses becomes extremely small, consistently with the dominance of slip-weakening behavior in the friction law.

4. Discussion

[50] Our dynamic rupture simulations generated a variety of rupture styles, which we classified following four distinct criteria: based on the stability of their peak slip rate, ruptures were classified as decaying, steady or growing ruptures; based on their risetime, as pulses or cracks; based on their rupture speed, as subshear or supershear; and based on their complexity, as single or multiple ruptures. Most of these rupture styles are consistent with those reported by previous numerical studies, laboratory experiments and earthquake observations, or predicted by previous theoretical studies. However, our simulation results provide a number of new insights. This section summarizes the new understandings of known rupture patterns and highlights the original rupture patterns revealed by our simulations. We discuss important implications of our findings for seismogenic processes and observational earthquake seismology, while mentioning limitations of our modeling assumptions. Also, we draw connections to recent observations which can be interpreted in the framework of our numerical findings.

4.1. The Initiation of Rupture

[51] Our results on the effect of nucleation size R_{max} provide insight into the conditions necessary for rupture initiation. The simulations by *Zheng and Rice* [1998] produced self-sustaining slip pulses only when the background stress was close to τ_{pulse}. By considering systematically the effect of nucleation size, we found that sustained rupture is possible at stresses lower than τ_{pulse}. Quantitatively, our results indicate that the nucleation size R_{max} required to initiate rupture depends exponentially on the relative strength S.

[52] A shortcoming of the simulations presented here is the artificial nature of the rupture initiation procedures employed, although in some of our models growing ruptures initiate from a steady state pulse far from the artificial nucleation regions. On the one hand, our results provide a basis for the design and interpretation of future studies that will incorporate more physical, spontaneous nucleation process through earthquake cycle simulations, although at a much higher computational cost [*Lapusta and Rice*, 2003; *Kaneko and Lapusta*, 2008; *Noda and Lapusta*, 2010]. On the other hand, we can propose a physical interpretation of our assumed nucleation procedure. *Aochi and Ide* [2005] envisioned a hierarchical spatial distribution of fault friction properties, in which small patches with fast weakening rate are embedded in large patches with slower weakening rate. Earthquakes nucleate on the smallest, most unstable patches, and might propagate to the largest patches by a cascade of dynamic triggering. In this context, our

simulations with uniform friction properties are focused on a single scale, and our imposed nucleation procedure is a proxy for the weakening induced by the rupture process at smaller scales. The compound size of the smaller patches in the nucleation region is parameterized in our model by the size of the imposed initiation zone, R_{max}.

[53] An interesting implication of this interpretation is related to the Gutenberg-Richter distribution of seismicity. At our modeling scale the fault is subjected to a steady sequence of nucleation attempts of various sizes, with smaller nucleation sizes (small R_{max}) being most likely. The steady state pulse is the self-sustained rupture style that requires the smallest R_{max}, and hence might appear as the most likely mode of rupture initiation [see also *Noda et al.*, 2009]. However, at low S, pulses are generated only over a narrow range of R_{max}, hence crack-like ruptures might be equally likely. As tectonic stress increases (decreasing S) the minimum nucleation size decreases dramatically (smaller R_{max} required for steady pulses) and the rate of successful nucleations should increase. This suggests that whether a rupture initiates as a crack or as a pulse depends on a competition between the tectonic loading rate and the background micro-seismicity rate. This competition should also affect the typical level of stress at the onset of large earthquakes, which ultimately controls stress drop and heat production.

4.2. Properties of Steady Pulses

[54] We found that the rupture speed, peak slip rate, risetime and cumulated slip of steady pulses increase as a function of S (Figure 6). Most of these trends were also found by *Perrin et al.* [1995] through an asymptotic analysis independent of nucleation assumptions, assuming a friction law with mild (logarithmic) dependence on slip velocity. The only difference is for risetimes, which they found to decrease with increasing S, probably reflecting a special sensitivity of the healing process to the assumed friction law.

[55] Decaying pulses could serve as a model for small earthquakes with spontaneous arrest. They can propagate a significant distance as steady state pulses before they decay. The inverse correlation found here between the rupture speed of steady pulses and the background stress level is similar to the inverse correlation between rupture speed and stress drop inferred by *Tan and Helmberger* [2010] from seismological observations of small earthquakes $(3 < M < 5)$ in the 2003 Big Bear aftershock sequence. Low rupture speeds at high stress also imply lower radiation efficiency [*Venkataraman and Kanamori*, 2004] for smaller magnitude events, which is a subject of debate in observational seismology. However, steady pulses are very sensitive to perturbations of small length scales, comparable to the pulse width, and may easily decay or transform into a growing pulse or crack if they encounter spatial heterogeneities of initial stresses or strength, which we have ignored in the present work.

4.3. Complex Ruptures Involving Multiple Fronts

[56] Our results provide further theoretical support to the existence of multiple earthquake rupture fronts, i.e. a fault patch may slip and stop more than once during the same earthquake. Complex ruptures with re-nucleation of slip after the passage of a pulse have been observed before in
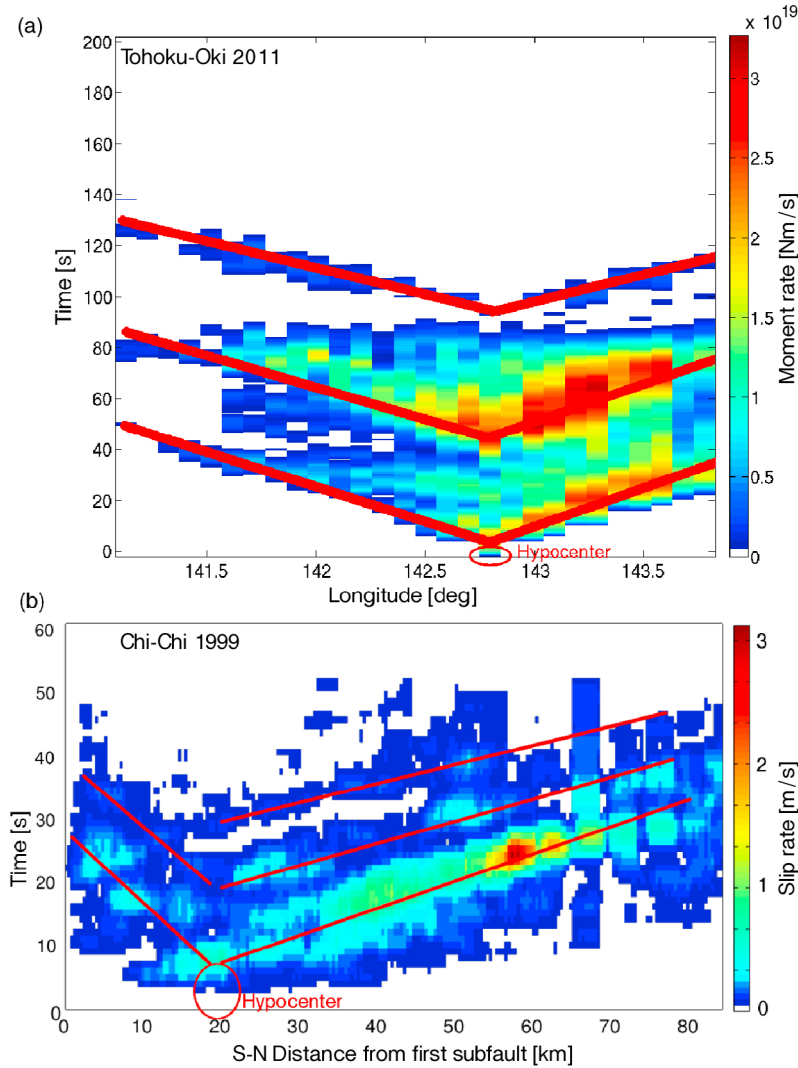
Figure 15. Re-activation of slip inferred for two large earthquakes. (a) The Tohoku-Oki (Japan) 2011 earthquake: spatiotemporal distribution of moment rate at the hypocentral latitude (38°) from the source inversion model by *Lee et al.* [2011] based on strong motion, teleseismic and GPS data. (b) The Chi-Chi (Taiwan) 1999 earthquake: spatiotemporal distribution of slip rate of all subfaults shallower than 10 km from the source inversion model by *Lee et al.* [2006]. For both events the source inversion assumes multiple time windows in slip rate. The red lines indicate interpreted multiple rupture fronts.

numerical simulations [*Cochard and Madariaga*, 1996; *Nielsen et al.*, 2000] and laboratory experiments [*Nielsen et al.*, 2010]. The mechanism for triggering secondary fronts was explained by *Nielsen and Madariaga* [2003] based on the analytical solution for a singular self-similar pulse. However, the identification of this complex rupture pattern in natural earthquakes requires source imaging at higher resolution than usually achieved by finite source inversion studies, which are limited to low frequencies and adopt restrictive assumptions about the rupture kinematics.

[57] For the 2011 M_w 9 Tohoku-Oki earthquake, an exceptionally well recorded large event, *Lee et al.* [2011] and *Yao et al.* [2011] suggested the occurrence of reactivated slip in the hypocentral region based, respectively, on source inversion of teleseismic, strong motion and geodetic data with a multiple-window parameterization of slip rate and on source imaging by back-projection of teleseismic

array data. While this inference is not present in other studies of the Tohoku-Oki earthquake, it warrants efforts to improve the resolution and robustness of source inversion and imaging techniques in order to distinguish rupture patterns of complexity comparable to that found in dynamic simulations. Similar episodes of multiple slip have been inferred for the 1999 Chi-Chi earthquake [*Lee et al.*, 2006] and the 1987 Superstitious Hills earthquake [*Wald et al.*, 1990]. In Figure 15 we visualize the relevant aspects of the source models of the Tohoku-Oki earthquake by *Lee et al.* [2011] and of the Chi-Chi earthquake by *Lee et al.* [2006]. We focus on a spatial cross-section of the source models to obtain a representation similar to our Figure 11a. These figures highlight the slip reactivation phenomenon: in both earthquakes one can clearly observe at least two distinct rupture fronts originating in the hypocentral area (indicated by red lines in Figure 15).

[58] Earthquakes are usually modeled as pulses in finite kinematic source inversions. However, risetime remains one of the least well constrained source parameters, which makes it difficult to distinguish between true cracks and pulses with a long but weak slip-rate tail. A further complication arises from the possibility of multiple ruptures: an apparent crack-like behavior could emerge as the low-frequency manifestation of a sequence of multiple pulses.

[59] If the stress left behind the primary pulse is relatively low, the secondary rupture is a growing pulse. The secondary pulse can itself trigger a tertiary rupture, and triggering may repeat multiple times leading to a sequence of self-similar pulses [*Cochard and Madariaga*, 1996; *Nielsen et al.*, 2000]. These multiple-pulse ruptures have a different origin than the "multipulse mode" or "train of pulses" observed in previous simulations [*Coker et al.*, 2005; *Lapusta*, 2005; *Shi et al.*, 2008]. Both phenomena appear under conditions close to the transition between (single) pulse-like and crack-like rupture. However, whereas the former requires a primary pulse and relative long re-nucleation times, the latter arises from an intrinsic instability present also for primary cracks [*Lapusta*, 2005] and involves short timescales between multiple rupture fronts. *Huang and Ampuero* [2011] proposed a mechanism for the generation of multiple pulses induced by reflected waves in the presence of a low velocity fault zone. In contrast, the mechanism described here does not require a heterogeneous elastic medium.

4.4. The Role of Multiple Ruptures on the Transition Between Pulses and Cracks

[60] Our results on multiple ruptures shed light into how an earthquake selects between the two basic rupture styles, crack and pulse. While theoretical studies determined that crack-like rupture is impossible when the background stress is below a critical value τ_{pulse} [*Zheng and Rice*, 1998; *Nielsen and Carlson*, 2000], at higher stress both rupture styles are possible and no recipe for rupture style selection is available. In contrast to the present work, previous numerical studies did not systematically investigate the effect of the size of the nucleation region. We found that the selection of rupture style does not only depend on the background stress, but also on the nucleation size R_{max}. The transition from pulse to crack as a function of increasing R_{max} involves a superposition of multiple rupture fronts, a pulse triggering a crack at the hypocenter. This result highlights the importance of the nucleation conditions for the character of the ensuing dynamic rupture.

4.5. Complex Ruptures Involving Back-Propagating Fronts

[61] Some of our models show back-propagating fronts. In Figure 11b, a weak steady pulse nucleates a stronger, bilateral rupture. One of the triggered fronts propagates back toward the hypocenter. Evidence of a rupture front propagating in the direction opposite to the overall rupture direction was reported for the 1984 Morgan Hill earthquake, based on strong motion observations [*Beroza and Spudich*, 1988], and for the 2011 El Mayor - Cucapah earthquake, based on an eyewitness account and on regional array back-projection [*Hudnut*, 2011; *Meng et al.*, 2011]. Proposed mechanisms involve the presence of heterogeneities of fault strength or stress. Our results suggest that back-propagating

ruptures are possible even on a fault with uniform initial stress and friction properties.

4.6. The Supershear Transition of Pulse-Like Ruptures

[62] To our knowledge, the supershear transition from pulse-like ruptures, predicted by the theoretical analysis of *Dunham* [2007] and observed in laboratory experiments [*Lu et al.*, 2007, 2009], is reported here for the first time in numerical simulations. However, in our models this phenomenon is confined to a narrow range of initial stress and nucleation conditions. The absence of fine tuning in the laboratory experiments might suggest that the critical stress for pulse-crack transition is closer to the critical stress for supershear transition than assumed in our simulations, i.e. S_{pulse} closer to $S_{ss} \approx 1$. This might imply $\mu V_c / \sigma (\mu_s - \mu_d)$ $c_S \approx 0.17$ (beyond the range explored here, ≤ 0.09). Further quantitative comparison between simulations and experiments also requires determination of the high-velocity frictional properties of the laboratory samples.

4.7. Properties of Supershear Ruptures

[63] In our velocity-weakening simulations the critical S for supershear transition is $S_{ss} \approx 1.2$. For self-similar ruptures propagating at near-Rayleigh speed (Figure 4), such low S_{ss} values are expected for pulses with near-Rayleigh healing front speed [*Dunham*, 2007, Figure 3], which is the case in our growing pulse simulations (Figure 8), but are not expected for cracks. Analytical solutions for the dynamic stresses induced by self-similar cracks indicate that $S_{ss} = 1.77$ (*Burridge* [1973], corrected by *Andrews* [1985]). To a large extent, the low S_{ss} in dynamic ruptures under velocity-weakening friction can be attributed to a limited applicability of the conventional definition of S, as elaborated in Appendix B. In addition, finite size effects also affect the apparent S_{ss}: as S approaches the true S_{ss} the supershear transition happens at a rupture distance larger than our computational domain and beyond our simulation time ($t \leq 1000$). The scarcity of supershear ruptures in nature implies that S is relatively high, but our results suggest that it is not straightforward to infer a more quantitative constraint on the lower bound of S.

[64] In laboratory experiments [*Lu et al.*, 2007] and in analytical studies [*Samudrala et al.*, 2002] the rupture speed was found to decrease with increasing S. *Lu et al.* [2009] found in laboratory experiments that supershear fronts generated by pulses propagated slower than those generated by cracks. The laboratory experiments may be dominated by transient response. In contrast, our simulation results are more asymptotic and show insignificant dependence of supershear rupture speed on S or on the style of the primary rupture. We also found that strong slip rate peaks are generated at the transition to supershear rupture. These should produce strong, high frequency radiation phases, perhaps observable in real earthquakes by back-projection source imaging.

5. Conclusions

[65] We conducted a systematic numerical study of 2D inplane dynamic rupture on faults governed by a rate-and-state-dependent friction law with severe velocity-weakening at high speed. Ruptures were artificially nucleated
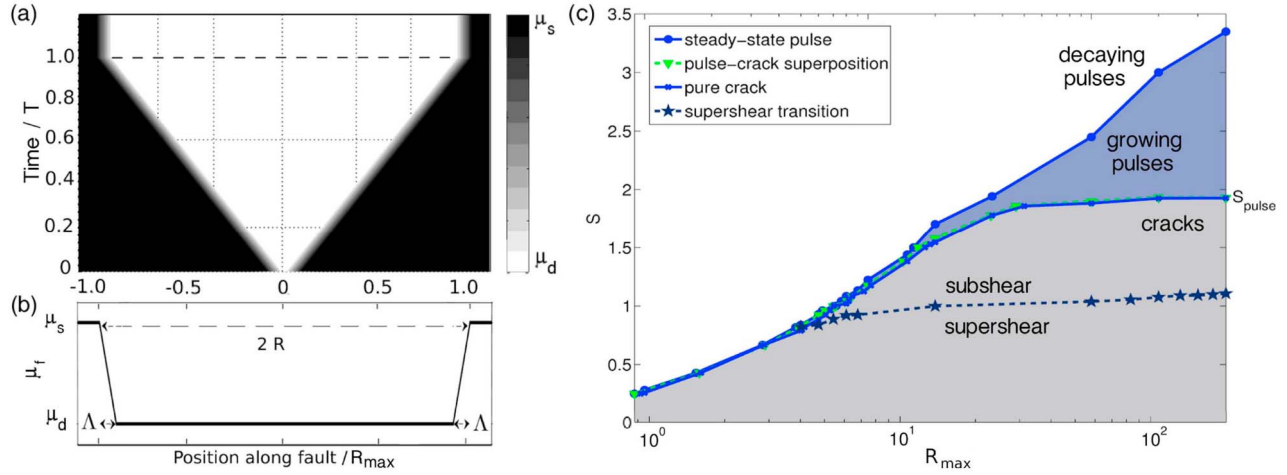
Figure A1. (a) Nucleation "procedure 2" without healing. It has duration T, expands at constant speed V_n, and reaches a maximum half-size $R_{max} = V_n T$. (b) Prescribed spatial distribution of μ_f at $t = T$. (c) Summary of rupture styles as a function of S and R_{max} for nucleation "procedure 2", similar to Figure 5.

by prescribing a time-weakening zone of time-dependent size. Our results show that ruptures can propagate with a variety of styles, which we classified by several criteria: stability (decaying, steady or growing behavior of peak slip rate), risetime (pulses or cracks), rupture speed (subshear or supershear), and complexity (single or multiple rupture fronts). We identified the effect of initial stress (relative strength parameter S), nucleation size (R_{max}) and characteristic weakening velocity (V_c) on the style of rupture, with special attention to the transitions between these styles as a function of S and R_{max}. The asymptotic properties (independent of nucleation) of steady state and self-similar pulses were quantified as a function of S. For steady state pulses, rupture speed, peak slip rate, risetime and cumulated slip increase with increasing S. For self-similar pulses, rupture speed and slip gradient decrease with increasing S, and the healing front speed does not depend significantly on S and remains close but slower than the Rayleigh speed.

[66] We found that rupture initiation requires a minimal nucleation size that depends exponentially on the relative strength S. The selection between crack and pulse behavior depends on the size of the nucleation zone. Our results support the possibility of repeated slip due to multiple rupture fronts during an earthquake, under conditions intermediate between pure pulse-like and crack-like behavior. Supershear ruptures under velocity-weakening friction require lower S than under slip-weakening, generate high-frequency radiation during transition and can be triggered also by initially pulse-like ruptures. Ruptures involving back-propagating fronts were also found. In an intrinsically heterogeneous natural environment, earthquakes may not be restricted to a single rupture style but rather involve complex rupture patterns with multiple rupture fronts and multiple styles. Even if some propagation styles transition soon into a style present over a larger parameter range, the physical transition processes and macroscopic source properties implied by each mode are important to understand. For example, we can speculate that if actual earthquakes start under minimal but favorable nucleation energies, the steady state pulse, a rupture style which is found only in a narrow

parameter range in our models, may well occur in actual earthquakes, at least transiently.

[67] Our study is limited to homogeneous initial stresses. While the fundamental rupture styles found here are expected to manifest themselves also under heterogeneous initial stresses, the robustness of the transition behaviors with respect to stress heterogeneities is an important question to be investigated in future work.

[68] The quantitative analysis of the conditions and physical mechanisms for a variety of rupture behavior is of interest for a broad audience in earthquake science, including laboratory studies of rock friction and seismological observations of earthquake source complexity. The complex rupture patterns studied here warrant further developments in earthquake source imaging. The detection of rupture style and its transitions may help elucidating the state of stress and strength of active fault zones. Our results will be a starting point to study the effect of rupture style on measurable earthquake source properties and strong ground motion.

Appendix A: Non-healing Nucleation

[69] We extend our study of the influence of nucleation on dynamic rupture style by considering a second, non-healing nucleation procedure. In this nucleation "procedure 2", we impose time-weakening without subsequent healing, as introduced by *Andrews* [1985]. The nucleation zone expands with constant rupture speed V_n up to duration T and final half-size $R_{max} = V_n T$:

$$R(t) = \begin{cases} V_n t & \text{for } 0 \leq t \leq T \\ R_{max} & \text{for } t \geq T. \end{cases} \quad (A1)$$

The shape of the nucleation zone resulting from equation (A1) is depicted in Figures 16a and 16b. Healing is prevented in the nucleation region. The previously introduced healing nucleation "procedure 1" and the newly defined non-healing "procedure 2" represent two extreme cases of frictional behavior: a transient weakening process with subsequent healing and an irreversible weakening process.
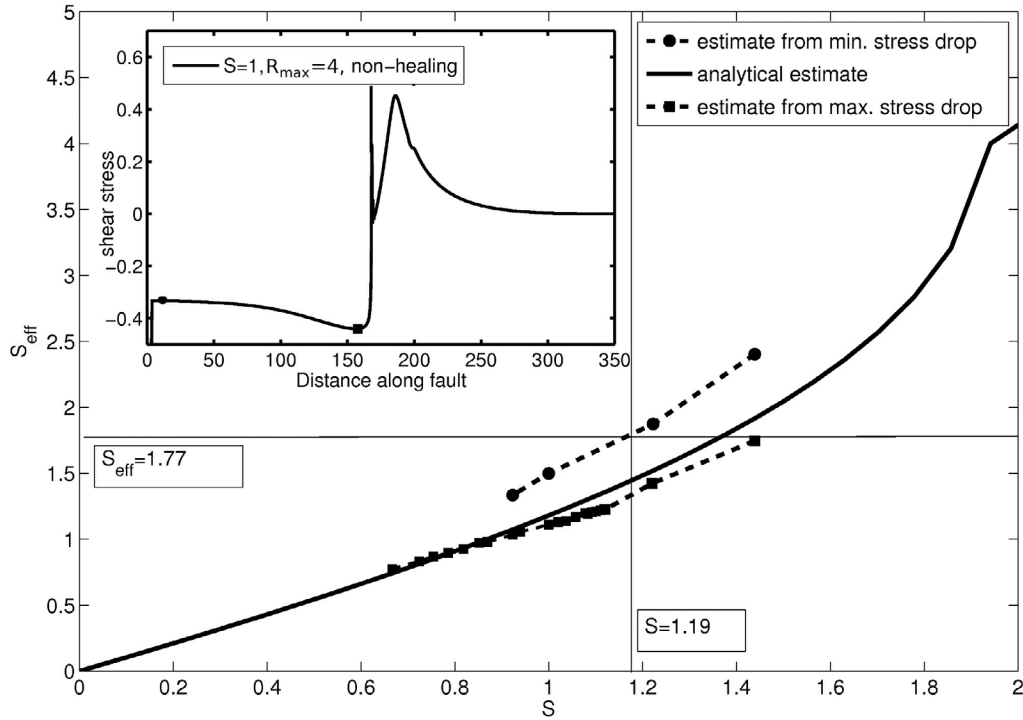
Figure B1. Theoretical estimate of an effective relative strength, S_{eff}, as a function of nominal S, compared to low and high bounds on effective S based on the minimal and maximal stress drop measured in the simulations. We consider only subshear cracks with values of S and R_{max} very close to the supershear transition. Inset: the shear stress distribution along the fault for a typical subshear crack.

[70] We ran the same set of simulations of section 2.5 applying the non-healing nucleation "procedure 2". We found that the nucleation type does not affect significantly the rupture transition processes. Both nucleation procedures result in the same qualitative dependence of rupture style on S and R_{max} (Figure A1c). They differ slightly in the size R_{max} required to trigger equivalent rupture styles at a given level of S. For example, "procedure 1" requires larger nucleations to reach steady state compared to "procedure 2", especially at small values of R_{max} for which the two procedures prescribe significantly different nucleation front evolutions. This can be attributed to the lesser amount of energy provided by "procedure 1" due to the onset of artificial healing. The range of values of R_{max} and S allowing sustained pulses is considerably narrower for "procedure 2" because it forces the nucleation region to remain weak even after the end of nucleation.

[71] Under nucleation "procedure 2", the absence of prescribed healing favors reactivation of slip at the hypocenter and the pulse-crack boundary in Figure A1c remains closer to S_{pulse} than with nucleation "procedure 1" (Figure 5).

Appendix B: On the Low Critical S Value for Supershear Transition

[72] We found in section 3.6 that the supershear transition requires $S < S_{ss} \approx 1$, significantly lower than under slip-weakening friction ($S_{ss} = 1.77$). We show here that such low S_{ss} values can be attributed to the typically incomplete dynamic strength drop under velocity-weakening friction, and attempt to derive a more appropriate predictor for supershear transition.

[73] The dynamic stress achieved in our simulations is higher than the nominal dynamic stress, τ_d, involved in the definition equation (7). The inset of Figure B1 shows that the dynamic stress inside a typical subshear crack reaches its minimum at the tail of the process zone and has a maximum near the hypocenter. To estimate higher and lower bounds on the effective S (S_{max} and S_{min}, respectively) we replace τ_d in equation (7) by, respectively, the maximum and minimum stress actually achieved inside a crack during a simulation. These bounds are reported in Figure B1 for a range of nominal S values. Remarkably, the low values $S_{ss} \approx 1$ in our velocity-weakening crack simulations correspond to $S_{max} \approx 1.77$, the critical value for slip-weakening cracks.

[74] To predict if a rupture will become supershear under a given background stress, we define an effective relative strength parameter S_{eff} that can be evaluated a priori. We replace the nominal stress drop $\tau_0 - \tau_d$ in equation (7) by an estimate of the stress drop at the center of a crack [*Zheng and Rice*, 1998]:

$$\Delta\tau = \mu V_{dyna}/2c_S \qquad (B1)$$

where V_{dyna} is the solution of

$$\tau_0 - \frac{\mu}{2c_S} V_{dyna} = \sigma\mu_{ss}(V_{dyna}) \qquad (B2)$$

The steady state friction coefficient μ_{ss} is given by equation (3). We found that S_{eff} is comparable to the lower bound S_{min} derived from the numerical simulations (Figure B1).

Appendix C: Fracture Mechanical Aspects of Rupture Speed and Peak Slip Velocity

[75] Insight on the evolution of peak slip rate V and rupture speed v_r as a function of propagation distance x is developed here from fracture mechanics considerations. The fracture energy dissipated by our adopted friction law is [*Ampuero and Ben-Zion*, 2008, equation C4]:

$$G_c = \sigma b D_c \frac{V}{V_c} \frac{\ln\left(1 + \frac{V}{V_c}\right)}{\left(1 + \frac{V}{V_c}\right)}. \tag{C1}$$

where V is the peak slip rate, reached near the trailing edge of the process zone. At large slip rate, $V \gg V_c$, we obtain

$$G_c(V) \approx \sigma b D_c \ln(V/V_c). \tag{C2}$$

[76] The balance between the energy release rate G and the fracture energy G_c provides an equation of motion for the rupture front [*Freund*, 1990]:

$$\frac{(\tau_0 - \tau_{min})^2 (1 - \nu)}{g(v_r) 2\mu} k^2(v_h, v_r) \, x = G_c(V) \tag{C3}$$

where x is the rupture propagation distance, $v_r = \dot{x}$ is the rupture speed, g is a dimensionless function of rupture speed and k is a dimensionless function of rupture speed and (for self-similar pulses) of healing speed v_h. Moreover, peak slip rate and rupture speed are related by *Ida* [1972]:

$$V \propto \frac{v_r(\tau_s - \tau_{min})(1 - \nu)}{g(v_r)\mu}. \tag{C4}$$

[77] For self-similar pulses and cracks $k^2/g \propto \sqrt{1 - v_r/c_R}$ and $g \propto \sqrt{1 - v_r/c_R}$ when $v_r \approx c_R$ [*Freund*, 1990; *Nielsen and Madariaga*, 2003], which implies:

$$x \propto \frac{\ln(V/V_c)}{\sqrt{1 - v_r/c_R}} \tag{C5}$$

$$V \propto \frac{v_r(\tau_s - \tau_{min})(1 - \nu)}{\sqrt{1 - v_r/c_R}\mu} \tag{C6}$$

We infer from this that the rupture speed of sub-shear cracks and growing pulses accelerates toward the Rayleigh speed c_R, and that the growth of peak slip rate as a function of rupture propagation distance satisfies the following relation:

$$V \ln(V/V_c) \propto x. \tag{C7}$$

Simple scaling factors in this relation seemingly provide fits for all rupture styles in our models (Figure 9).

References

Ampuero, J. P. (2008), *SEM2DPACK: A spectral element method tool for 2D wave propagation and earthquake source dynamics*, User's guide, version 2.3.0, Calif. Inst. of Technol., Pasadena.

Ampuero, J. P., and Y. Ben-Zion (2008), Cracks, pulses and macroscopic asymmetry of dynamic rupture on a bimaterial interface with velocity-weakening friction, *Geophys. J. Int.*, *173*(2), 674–692, doi:10.1111/j.1365-246X.2008.03736.x.

Andrews, D. (1985), Dynamic plane-strain shear rupture with a slip-weakening friction law calculated by a boundary integral method, *Bull. Seismol. Soc. Am.*, *75*(1), 1–21, doi:10.1.1.114.5819.

Andrews, D. J. (1976), Rupture velocity of plane strain shear cracks, *J. Geophys. Res.*, *81*, 5679–5689, doi:10.1029/JB081i032p05679.

Andrews, D. J. (1999), Test of two methods for faulting in finite-difference calculations, *Bull. Seismol. Soc. Am.*, *89*(4), 931–937.

Andrews, D. J., and Y. Ben-Zion (1997), Wrinkle-like slip pulse on a fault between different materials, *J. Geophys. Res.*, *102*, 553–572, doi:10.1029/96JB02856.

Aochi, H., and S. Ide (2005), Earthquakes as multiscale dynamic ruptures with heterogeneous fracture surface energy, *J. Geophys. Res.*, *110*, B11303, doi:10.1029/2004JB003591.

Archuleta, R. J. (1984), A faulting model for the 1979 Imperial Valley earthquake, *J. Geophys. Res.*, *89*, 4559–4586, doi:10.1029/JB089iB06p04559.

Beeler, N. M., and T. E. Tullis (1996), Self-healing slip pulses in dynamic rupture models due to velocity-dependent strength, *Bull. Seismol. Soc. Am.*, *86*(4), 1130–1148.

Beeler, N., T. Tullis, and D. Goldsby (2008), Constitutive relationships and physical basis of fault strength due to flash heating, *J. Geophys. Res.*, *113*, B01401, doi:10.1029/2007JB004988.

Beroza, G. C., and T. Mikumo (1996), Short slip duration in dynamic rupture in the presence of heterogeneous fault properties, *J. Geophys. Res.*, *101*, 22,449–22,460, doi:10.1029/96JB02291.

Beroza, G. C., and P. Spudich (1988), Linearized inversion for fault rupture behavior: Application to the 1984 Morgan Hill, California, earthquake, *J. Geophys. Res.*, *93*(B6), 6275–6296, doi:10.1029/JB093iB06p06275.

Bizzarri, A. (2010), How to promote earthquake ruptures: Different nucleation strategies in a dynamic model with slip-weakening friction, *Bull. Seismol. Soc. Am.*, *100*, 923–940, doi:10.1785/0120090179.

Bouchon, M., H. Karabulut, M.-P. Bouin, J. Schmittbuhl, M. Vallée, R. Archuleta, S. Das, F. Renard, and D. Marsan (2010), Faulting characteristics of supershear earthquakes, *Tectonophysics*, *493*(3–4), 244–253, doi:10.1016/j.tecto.2010.06.011.

Brune, J. N. (1970), Tectonic stress and the spectra of seismic shear waves from earthquakes, *J. Geophys. Res.*, *75*(26), 4997–5009, doi:10.1029/JB075i026p04997.

Burridge, R. (1973), Admissible speeds for plane-strain self-similar shear cracks with friction but lacking cohesion, *Geophys. J. Int.*, *35*, 439–455, doi:10.1111/j.1365-246X.1973.tb00608.x.

Campillo, M., J. C. Gariel, K. Aki, and F. J. Sanchez-Sesma (1989), Destructive strong ground motion in Mexico city: Source, path, and site effects during great 1985 Michoacan earthquake, *Bull. Seismol. Soc. Am.*, *79*(6), 1718–1735.

Cochard, A., and R. Madariaga (1994), Dynamic faulting under rate-dependent friction, *Pure Appl. Geophys.*, *142*(3–4), 419–445, doi:10.1007/BF00876049.

Cochard, A., and R. Madariaga (1996), Complexity of seismicity due to highly rate-dependent friction, *J. Geophys. Res.*, *101*(B11), 25,321–25,336, doi:10.1029/96JB02095.

Coker, D., G. Lykotrafitis, A. Needleman, and A. Rosakis (2005), Frictional sliding modes along an interface between identical elastic plates subject to shear impact loading, *J. Mech. Phys. Solids*, *53*(4), 884–922, doi:10.1016/j.jmps.2004.11.003.

Dalguer, L. A., and S. M. Day (2007), Staggered-grid split-node method for spontaneous rupture simulation, *J. Geophys. Res.*, *112*, B02302, doi:10.1029/2006JB004467.

Dalguer, L. A., and S. M. Day (2009), Asymmetric rupture of large aspect-ratio faults at bimaterial interface in 3D, *Geophys. Res. Lett.*, *36*, L23307, doi:10.1029/2009GL040303.

Das, S., and K. Aki (1977a), A numerical study of two-dimensional spontaneous rupture propagation, *Geophys. J. R. Astron. Soc.*, *50*(3), 643–668, doi:10.1111/j.1365-246X.1977.tb01339.x.

Das, S., and K. Aki (1977b), Fault plane with barriers: A versatile earthquake model, *J. Geophys. Res.*, *82*(36), 5658–5670, doi:10.1029/JB082i036p05658.

Day, S. M. (1982), Three-dimensional finite difference simulation of fault dynamics: Rectangular faults with fixed rupture velocity, *Bull. Seismol. Soc. Am.*, *72*(3), 705–727.

Day, S. M., and G. P. Ely (2002), Effect of a shallow weak zone on fault rupture: Numerical simulation of scale-model experiments, *Bull. Seismol. Soc. Am.*, *92*(8), 3022–3041, doi:10.1785/0120010273.

Day, S. M., G. Yu, and D. J. Wald (1998), Dynamic stress changes during earthquake rupture, *Bull. Seismol. Soc. Am.*, *88*(2), 512–522.

Di Carli, S., C. François-Holden, S. Peyrat, and R. Madariaga (2010), Dynamic inversion of the 2000 Tottori earthquake based on elliptical subfault approximations, *J. Geophys. Res.*, *115*, B12328, doi:10.1029/2009JB006358.

Di Toro, G., T. Hirose, S. Nielsen, G. Pennacchioni, and T. Shimamoto (2005), Natural and experimental evidence of melt lubrication of faults during earthquakes, *Eos Trans. AGU*, *86*(52), Fall Meet. Suppl., Abstract T13E-02.

Dunham, E. (2007), Conditions governing the occurrence of supershear ruptures under slip-weakening friction, *J. Geophys. Res.*, *112*, B07302, doi:10.1029/2006JB004717.

Dunham, E. M., and R. J. Archuleta (2004), Evidence for a supershear transient during the 2002 Denali Fault Earthquake, *Bull. Seismol. Soc. Am.*, *94*(6B), S256–S268, doi:10.1785/0120040616.

Dunham, E. M., D. Belanger, L. Cong, and J. E. Kozdon (2011), Earthquake ruptures with strongly rate-weakening friction and off-fault plasticity: 1. Planar faults, *Bull. Seismol. Soc. Am.*, *101*(5), 2296–2307, doi:10.1785/0120100075.

Festa, G., and J. Vilotte (2006), Influence of the rupture initiation on the intersonic transition: Crack-like versus pulse-like modes, *Geophys. Res. Lett.*, *33*, L15320, doi:10.1029/2006GL026378.

Freund, L. (1990), *Dynamic Fracture Mechanics*, *Cambridge Monogr. Mech. Appl. Math.*, Cambridge Univ. Press, Cambridge.

Harris, R. A., et al. (2004), The source physics of large earthquakes: Validating spontaneous rupture methods, *Eos Trans. AGU*, *85*(47), Fall Meet. Suppl., Abstract S12A-05.

Heaton, T. H. (1990), Evidence for and implications of self-healing pulses of slip in earthquake rupture, *Phys. Earth Planet. Inter.*, *64*(1), 1–20, doi:10.1016/0031-9201(90)90002-F.

Heaton, T., S. Minson, and M. Simons (2011), Characterization of the slip pulse for the 2010 M 8.8 Maule earthquake, Abstract S11A-2193 presented at 2011 Fall Meeting, AGU, San Francisco, Calif., 5–9 Dec.

Hirose, T., and T. Shimamoto (2005), Slip-weakening distance of faults during frictional melting as inferred from experimental and natural pseudotachylytes, *Bull. Seismol. Soc. Am.*, *95*(5), 1666–1673, doi:10.1785/0120040131.

Huang, Y., and J.-P. Ampuero (2011), Pulse-like ruptures induced by low-velocity fault zones, *J. Geophys. Res.*, *116*, B12307, doi:10.1029/2011JB008684.

Hudnut, K. W. (2011), The 4 April 2010 El Mayor-Cucapah earthquake source, from initial glimpse to synoptic overview, paper presented at the 2011 SCEC Annual Meeting, South. Calif. Earthquake Cent., Palm Springs, 11–14 Sept. [Available at http://www.scec.org/meetings/2011am/emc.html.]

Ida, Y. (1972), Cohesive force across the tip of a longitudinal-shear crack and Griffith's specific surface energy, *J. Geophys. Res.*, *77*(20), 3796–3805, doi:10.1029/JB077i020p03796.

Ide, S., G. C. Beroza, and J. J. McGuire (2005), Imaging earthquake source complexity, in *Seismic Earth: Array Analysis of Broadband Seismograms*, *Geophys. Monogr. Ser.*, vol. 157, edited by A. Levander and G. Nolet, pp. 117–135, AGU, Washington, D. C.

Johnson, E. (1992), The influence of the lithospheric thickness on bilateral slip, *Geophys. J. Int.*, *108*, 151–160, doi:10.1111/j.1365-246X.1992.tb00846.x.

Kaneko, Y., and N. Lapusta (2008), Variability of earthquake nucleation in continuum models of rate-and-state faults and implications for aftershock rates, *J. Geophys. Res.*, *113*, B12312, doi:10.1029/2007JB005154.

Kaneko, Y., and N. Lapusta (2010), Supershear transition due to a free surface in 3D simulations of spontaneous dynamic rupture on vertical strike-slip faults, *Tectonophysics*, *493*(3–4), 272–284, doi:10.1016/j.tecto.2010.06.015.

Kaneko, Y., N. Lapusta, and J.-P. Ampuero (2008), Spectral element modeling of spontaneous earthquake rupture on rate and state faults: Effect of velocity-strengthening friction at shallow depths, *J. Geophys. Res.*, *113*, B09317, doi:10.1029/2007JB005553.

Komatitsch, D., and J. Tromp (1999), Introduction to the spectral-element method for 3-D seismic wave propagation, *Geophys. J. Int.*, *139*(3), 806–822, doi:10.1046/j.1365-246x.1999.00967.x.

Komatitsch, D., and J. P. Vilotte (1998), The spectral-element method: An efficient tool to simulate the seismic response of 2D and 3D geological structures, *Bull. Seismol. Soc. Am.*, *88*(2), 368–392.

Kostrov, B. V. (1964), Self similar problems of propagation of shear cracks, *J. Appl. Math. Mech.*, *28*(5), 1077–1087, doi:10.1016/0021-8928(64)90010-3.

Lapusta, N. (2005), Modes of dynamic rupture on interfaces with nonlinear rate and state friction laws, paper presented at 11th International Conference on Fracture, Ital. Group of Fracture, Turin, Italy.

Lapusta, N., and J. R. Rice (2003), Nucleation and early seismic propagation of small and large events in a crustal earthquake model, *J. Geophys. Res.*, *108*(B4), 2205, doi:10.1029/2001JB000793.

Lee, S.-J., K.-F. Ma, and H.-W. Chen (2006), Three-dimensional dense strong motion waveform inversion for the rupture process of the 1999 Chi-Chi, Taiwan, earthquake, *J. Geophys. Res.*, *111*, B11308, doi:10.1029/2005JB004097.

Lee, S.-J., B.-S. Huang, M. Ando, H.-C. Chiu, and J.-H. Wang (2011), Evidence of large scale repeating slip during the 2011 Tohoku-Oki earthquake, *Geophys. Res. Lett.*, *38*, L19306, doi:10.1029/2011GL049580.

Lu, X., N. Lapusta, and A. J. Rosakis (2007), Pulse-like and crack-like ruptures in experiments mimicking crustal earthquakes, *Proc. Natl. Acad. Sci. U. S. A.*, *104*(48), 18,931–18,936, doi:10.1073/pnas.0704268104.

Lu, X., N. Lapusta, and A. J. Rosakis (2009), Analysis of supershear transition regimes in rupture experiments: The effect of nucleation conditions and friction parameters, *Geophys. J. Int.*, *177*, 717–732, doi:10.1111/j.1365-246X.2009.04091.x.

Lykotrafitis, G., A. J. Rosakis, and G. Ravichandran (2006), Self-healing pulse-like shear ruptures in the laboratory, *Science*, *313*(5794), 1765–1768, doi:10.1126/science.1128359.

Madariaga, R. I., C. Vigny, M. Lancieri, S. Ruiz, J. A. Campos, and The Montessus de Ballore International Laboratory (2010), The February 27, 2010 Mw 8.8 Maule earthquake as observed by cGPS and strong motion instruments, Abstract U21B-03 presented at 2010 Fall Meeting, AGU, San Francisco, Calif., 13–17 Dec.

Mavroeidis, G. P., and A. S. Papageorgiou (2010), Effect of fault rupture characteristics on near-fault strong ground motions, *Bull. Seismol. Soc. Am.*, *100*(1), 37–58, doi:10.1785/0120090018.

Meng, L., J.-P. Ampuero, M. T. Page, and K. W. Hudnut (2011), Seismological evidence and dynamic model of reverse rupture propagation during the 2010 M7.2 El Mayor - Cucapah earthquake, Abstract S52B-04 presented at 2011 Fall Meeting, AGU, San Francisco, Calif., 5–9 Dec.

Nielsen, S., and R. Madariaga (2003), On the self-healing fracture mode, *Bull. Seismol. Soc. Am.*, *93*(6), 2375–2388.

Nielsen, S., G. Di Toro, T. Hirose, and T. Shimamoto (2008), Frictional melt and seismic slip, *J. Geophys. Res.*, *113*, B01308, doi:10.1029/2007JB005122.

Nielsen, S., J. Taddeucci, and S. Vinciguerra (2010), Experimental observation of stick–slip instability fronts, *Geophys. J. Int.*, *180*(2), 697–702, doi:10.1111/j.1365-246X.2009.04444.x.

Nielsen, S. B., and J. M. Carlson (2000), Rupture pulse characterization: Self-healing, self-similar, expanding solutions in a continuum model of fault dynamics, *Bull. Seismol. Soc. Am.*, *90*(6), 1480–1497, doi:10.1785/0120000021.

Nielsen, S. B., and K. B. Olsen (2000), Constraints on stress and friction from dynamic rupture models of the 1994 Northridge, California, earthquake, *Pure Appl. Geophys.*, *157*, 2029–2046, doi:10.1007/PL00001073.

Nielsen, S. B., J. M. Carlson, and K. B. Olsen (2000), Influence of friction and fault geometry on earthquake rupture, *J. Geophys. Res.*, *105*(B3), 6069–6088, doi:10.1029/1999JB900350.

Noda, H., and N. Lapusta (2010), Three-dimensional earthquake sequence simulations with evolving temperature and pore pressure due to shear heating: Effect of heterogeneous hydraulic diffusivity, *J. Geophys. Res.*, *115*, B12314, doi:10.1029/2010JB007780.

Noda, H., E. M. Dunham, and J. R. Rice (2009), Earthquake ruptures with thermal weakening and the operation of major faults at low overall stress levels, *J. Geophys. Res.*, *114*, B07302, doi:10.1029/2008JB006143.

Oglesby, D. D., and S. M. Day (2002), Stochastic fault stress: Implications for fault dynamics and ground motion, *Bull. Seismol. Soc. Am.*, *92*(8), 3006–3021.

Page, M., P. M. Mai, and D. Schorlemmer (2011), Testing earthquake source inversion methodologies, *Eos Trans. AGU*, *92*, 75, doi:10.1029/2011EO090007.

Perrin, G., J. R. Rice, and G. Zheng (1995), Self-healing slip pulse on a frictional surface, *J. Mech. Phys. Solids*, *43*(9), 1461–1495, doi:10.1016/0022-5096(95)00036-I.

Peyrat, S., K. Olsen, and R. Madariaga (2001), Dynamic modeling of the 1992 Landers earthquake, *J. Geophys. Res.*, *106*, 26,467–26,482, doi:10.1029/2001JB000205.

Rice, J. R. (2006), Heating and weakening of faults during earthquake slip, *J. Geophys. Res.*, *111*, B05311, doi:10.1029/2005JB004006.

Samudrala, O., Y. Huang, and A. J. Rosakis (2002), Subsonic and intersonic shear rupture of weak planes with a velocity weakening cohesive zone, *J. Geophys. Res.*, *107*(B8), 2170, doi:10.1029/2001JB000460.

Shi, Z., Y. Ben-Zion, and A. Needleman (2008), Properties of dynamic rupture and energy partition in a solid with a frictional interface, *J. Mech. Phys. Solids*, *56*(1), 5–24, doi:10.1016/j.jmps.2007.04.006.

Spudich, P., and E. Cranswick (1984), Direct observation of rupture propagation during the 1979 imperial valley earthquake using a short baseline accelerometer array, *Bull. Seismol. Soc. Am.*, *74*(6), 2083–2114.

Tan, Y., and D. Helmberger (2010), Rupture directivity characteristics of the 2003 Big Bear sequence, *Bull. Seismol. Soc. Am.*, *100*(3), 1089–1106, doi:10.1785/0120090074.

Templeton, E. L., and J. R. Rice (2008), Off-fault plasticity and earthquake rupture dynamics: 1. Dry materials or neglect of fluid pressure changes, *J. Geophys. Res.*, *113*, B09306, doi:10.1029/2007JB005529.

Tsutsumi, A., and T. Shimamoto (1997), High-velocity frictional properties of gabbro, *Geophys. Res. Lett.*, *24*(6), 699–702, doi:10.1029/97GL00503.

Tullis, T. E., and D. L. Goldsby (2003), Flash melting of crustal rocks at almost seismic slip rates, *Eos Trans. AGU*, *84*(46), Fall Meet. Suppl., Abstract S51B-05.

Venkataraman, A. and H. Kanamori (2004), Observational constraints on the fracture energy of subduction zone earthquakes, *J. Geophys. Res.*, *109*, B05302, doi:10.1029/2003JB002549.

Wald, D. J., D. V. Helmberger, and S. H. Hartzell (1990), Rupture process of the 1987 Superstition Hills Earthquake from the inversion of strong-motion data, *Bull. Seismol. Soc. Am.*, *80*(5), 1079–1098.

Wibberley, C. A. J., and T. Shimamoto (2005), Earthquake slip weakening and asperities explained by thermal pressurization, *Nature*, *436*, 689–692, doi:10.1038/nature03901.

Xia, K., A. J. Rosakis, and H. Kanamori (2004), Laboratory earthquakes: The sub-Rayleigh-to-supershear rupture transition, *Science*, *303*, 1859–1862, doi:10.1126/science.1094022.

Yao, H., P. Gerstoft, P. M. Shearer, and C. Mecklenbräuker (2011), Compressive sensing of the Tohoku-Oki Mw 9.0 earthquake: Frequency-dependent rupture modes, *Geophys. Res. Lett.*, *38*, L20310, doi:10.1029/2011GL049223.

Yomogida, K. (1988), Crack-like rupture processes observed in near-fault strong motion data, *Geophys. Res. Lett.*, *15*, 1223–1226, doi:10.1029/GL015i011p01223.

Zheng, G., and J. Rice (1998), Conditions under which velocity-weakening friction allows a self-healing versus a cracklike mode of rupture, *Bull. Seismol. Soc. Am.*, *88*(6), 1466–1483.